Revision of the paper "Continental pollution in the Western Mediterranean Basin: large variability of the aerosol single scattering albedo and influence on the direct shortwave radiative effect" by C. Di Biagio et al.

At first, we would like to thank the reviewers for having read the paper and provided valuable comments which helped to improve the quality of the manuscript. We have taken into consideration all the questions raised by the reviewers, and changed the paper accordingly. The details of our changes are highlighted in the text. The point by point answers to Reviewer #1 and #2 are provided in the following.

Some other minor changes, mostly regarding typos or grammar issues, were performed throughout the text. I also decided to refer to the "SkyGRIMM" only as "GRIMM" to be consistent with the spelling used in Di Biagio et al. (2015):

Di Biagio, C., et al.: Continental pollution in the western Mediterranean basin: vertical profiles of aerosol and trace gases measured over the sea during TRAQA 2012 and SAFMED 2013, Atmos. Chem. Phys., 15, 9611-9630, doi:10.5194/acp-15-9611-2015, 2015.

Reviewer #1

Line 78: Change ". . .aerosol optical properties represents one the main source. . ." to ". . .aerosol optical properties represents the main source. . ."
Done

Line 80: Change "In this sense, intensive studies providing with the characterization. . ." to "In this sense, intensive studies providing the characterization. . ."
Done

Line 86: Rephrase ". . .which makes that anthropogenic..", it doesn't make sense as is.
The sentence has been rewritten as: "On its northern bound, it is limited by Europe, with a consequent frequent export of anthropogenic pollution from the continent towards the basin (Lelieveld et al., 2002; Pace et al., 2006"

Lines 461-520 (Section 4.4): Since you use the refractive index to derive the size distribution, it would be better to take this into account in your "optical closure" process: change the size distribution based on the retrieved refractive index and see if you achieve the optical closure for the new size distribution. If not, retrieve a new refractive index using the new size distribution and the measured optical properties, change the size distribution based on the new refractive index and continue the process until you achieve the closure. I think that especially the large range of the imaginary part of the refractive index should have a distinctive effect on the derived size distribution and, consequently, on your optical closure procedure. If not, please provide relevant evidence.

I agree with the reviewer that this iterative approach is more appropriate and I applied it in this study to estimate the size distribution and refractive index of pollution aerosols. The details of the procedure are reported in Sect. 3.2 and illustrated in the new Figure 2. The results are discussed in the new Sect. 4.4: "Complex refractive index of pollution aerosols".

By applying the new retrieval procedure I obtain larger values (<20-50% increase) of both n and k at all wavelengths for five of the eight SLRr analysed, while no changes in the spectral refractive index are obtained in the other three cases. Conversely, no major changes are observed in the size distribution as a result of the iterative optical-to-geometrical refractive index correction (Fig. 4).

Due to the new retrieval, the results in Table 3 and Figures 4, 8, and 9 have also slightly changed.

Lines 485-490: How do the retrieved values of n and k compare with the ones used to derive the size distribution from PCASP and GRIMM measurements? Provide a comparison in a plot.

The optical-to-geometrical diameter conversion is now performed iteratively as explained in Sect. 3.2 and in the previous answer. In any case, the old values used to correct the PCASP and SkyGrimm data (n=1.50÷1.72 and k=0.01 at 632.8 and 655 nm, i.e. the operating wavelengths of the PCASP and the SkyGrimm) were in the range of variability of the obtained n and k by optical closure. In particular, k was at the mean of the estimated imaginary parts of the refractive index for the different cases at 660 nm. We can thus argue that the former approach used to perform the optical-to-geometrical diameter correction could be valuable to represent the "average" aerosol, as observed in this study.

Reviewer #2

The manuscript by Di Biagio et al. presents particle number size distributions, aerosol scattering and absorption coefficients and the derived quantities, which were performed in the course of the seventeen flights during the TRAQA campaign. The objective of the paper solves a well-defined questions: what is the heterogeneity on the optical properties in the Mediterranean Basin? and, how the observed variability is influencing in the evaluation of the radiative efficiency? To response these two questions, an analysis of the single scattering albedo is used.

The topic of the paper is suitable for ACP, the paper is well written and structured, the experimental approach is sound, and the data interpretation is reasonable. Then, the reviewer recommends the manuscript for publication with minor revisions: for which I give some suggestions below.

Specific comments:

Line 268: Please, modify the sentence: 'The total particle number concentration in the Aitken (4nm-0.1 um; dNAitken). . .' to 'The total particle number concentration in the ultrafine (4nm-0.1nm; dNUFP). . .'. It is because nucleation mode is (4-30) nm and Aitken mode is (30-100)nm. Nucleation+Aitken modes is called the ultrafine mode (UFP= UltraFine Particles). Modify the term dNAitkento dNUFP throughout the manuscript.

We replaced Aitken with UFP throughout the manuscript.

Line 387: please, check the reference section. Some references are missed (e.g. Toledano et al., 2007).

I checked the reference list and added missing references.

Lines 421-422 and Table 3: include the correlation coefficient between observed and fitted size distribution with the aim to analyze the goodness of fit function value.

The correlation coefficient is larger than 0.97 for all analysed cases. We have added this information in the main text: "The correlation coefficient for the fit functions is larger than 0.97 for all cases." (Sect. 4.2).

Section 4.2 and Figure 3: Number and volume size distributions in terms on the different air mass origin will be welcome.

Figure 3 has been redrawn by separating the data based on the origin of the sampled air masses. Also, the following text has been added in Section 4.2, as a comment to the new figure: "The minimum of the size distribution over the whole diameter range was measured in the Western sector (V32_R3), whilst the largest number concentrations in the super-micron range were observed in correspondence of V19_R1 and V32_R1. For all the other SLRs, the size distributions were very similar, especially at diameters below ~5 μm.".

Lines 430-433: The single scattering albedo increasing with wavelength may also suggest

a desert dust contribution. For dust particles, the scattering is fairly constant with wavelength so the SSA matches the decrease in absorption with wavelength (e.g. see Bergstrom et al., 2007 in ACP).

We have modified the text as:

"For these cases also very high values of ω were observed (0.92-0.97 for V19_R1 and 0.98-1.0 for V30_R2), which may suggest the possible mixing of pollution with sea spray or desert dust particles, both showing low absorption in the shortwave range (Bergstrom et al., 2007)."

The Abstract has been modified accordingly.

Figure 5: What is the meaning of the horizontal bars? Please, indicate in the Figure legend.

Horizontal bars represent the uncertainty on the measured/retrieved quantities shown in the plot. This has been specified in the figure caption.

Figure 6: please, check the comment for Figure 5.

See the previous answer.

During the revision we detected an error with the error-bars (which were inverted between the x and the y axes). We corrected this and also, for the sake of clarity, we decided only to show horizontal bars (measurements uncertainties) in the plot.

Continental pollution in the Western Mediterranean basin: large variability of the aerosol single scattering albedo and influence on the direct shortwave radiative effect

C. Di Biagio[1], P. Formenti[1], L. Doppler[2], C. Gaimoz[1], N. Grand[1], G. Ancellet[3], J.-L. Attié[4,5],

S. Bucci[6,7], P. Dubuisson[8], F. Fierli[6], M. Mallet[5], and F. Ravetta[3]

[1] *LISA, UMR CNRS 7583, Université Paris Est Créteil et Université Paris Diderot, Institut Pierre Simon Laplace, Créteil, France*

[2] *Deutscher Wetterdienst, Metorological Observatory Lindenberg, Germany*

[3] *Sorbonne Universités, UPMC Univ. Paris 06; Université Versailles St-Quentin; CNRS/INSU, LATMOS-IPSL, Paris, France*

[4] *Laboratoire d'Aérologie, University of Toulouse, UMR 5560 CNRS, France*

[5] *CNRM ~~GAME~~ UMR 3589, Météo-France/CNRS, Toulouse, France~~METEO-FRANCE~~*

[6] *Institute for Atmospheric Sciences and Climate of the National Research Council , (ISAC-CNR), Rome, 00133, Italy*

[7] *Sc. Dept. of Physics, Ferrara University, Ferrara, 44121, Italy*

[8] *Laboratoire d'Optique Atmosphérique, Université Lille ~~I~~, Villeneuve d'Ascq, 59655 Cedex, France*

Correspon~~id~~ence to~~ng author~~:

C. Di Biagio (claudia.dibiagio@lisa.u-pec.fr) and ~~Claudia Di Biagio,~~ P. Formenti (paola.formenti@lisa.u-pec.fr)

34 **Abstract**

35 Pollution aerosols strongly influence the composition of the Western Mediterranean basin,

36 but at present little is known on their optical properties. We report in this study in situ

37 observations of the single scattering albedo (ω) of pollution aerosol plumes measured over

38 the Western Mediterranean basin during the TRAQA (TRansport and Air QuAlity) airborne

39 campaign in summer 2012. Cases of pollution export from different source regions around

40 the basin and at different altitudes between ~160 and 3500 m above sea level ~~have been~~were

41 sampled during the flights. Data from this study show a large variability of ω, with values

42 between 0.84-0.98 at 370 nm and 0.70-0.99 at 950 nm. The single scattering albedo generally

43 decreases with the wavelength, with some exception associated to the mixing of pollution

44 with sea spray or dust particles over the sea surface. The ~~l~~Lowest values of ω (0.84-0.70

45 between 370 and 950 nm) are measured in correspondence of a fresh plume possibly linked

46 to ship emissions over the basin. The range of variability of ω observed in this study seems to

47 be independent of the source region around the basin, as well as of the altitude and ag~~e~~ing

48 time of the plumes. The observed variability of ω reflects in a large variability for the

49 complex refractive index of pollution aerosols, which is estimated to span in the large range

50 1.41-1.75 and 0.002-0.068 for the real and the imaginary parts, respectively, between 370 and

51 950 nm.

52 Radiative calculations in clear-sky conditions ~~have been~~were performed with the GAME

53 radiative transfer model to test the sensitivity of the aerosol shortwave Direct Radiative

54 Effect (DRE) to the variability of ω as observed in this study. Results from the calculations

55 suggest up to a 50% and 30% change of the forcing efficiency (FE), i.e. the DRE per unit of

56 optical depth, at the surface ($-160 \div -235$ $Wm^{-2}\tau^{-1}$ at 60° solar zenith angle) and at the Top-Of-

57 Atmosphere ($-137 \div -92$ $Wm^{-2}\tau^{-1}$) for ω varying between its maximum and minimum value.

58 This induces a change of up to an order of magnitude ($+23 \div +143$ $Wm^{-2}\tau^{-1}$) for the radiative

59 effect within the atmosphere.

60

61

62 **Keywords**: pollution aerosols, single scattering albedo, direct radiative effect, Western

63 Mediterranean

64

65

66

67

1. **Introduction**

Atmospheric aerosols play a crucial role on climate by affecting the radiative transfer of atmospheric radiation and by modifying cloud properties and lifetime (Boucher et al., 2013). The capability of atmospheric aerosols to interact through processes of scattering and absorption with the atmospheric radiation, so to exert a direct radiative effect (DRE), depends on their spectral optical properties (extinction efficiency, k_{ext}, single scattering albedo, ω, and asymmetry factor, g). In particular the single scattering albedo has been demonstrated to be a key parameter in modulating the surface, Top-of-Atmosphere (TOA), and atmospheric aerosol DRE (e.g., Ramana and Ramanathan, 2006; Di Biagio et al., 2010; Loeb and Su, 2010). Aerosol optical properties can largely vary depending on the particles composition, size distribution, and shape, which are function of the aerosol source, type, and processing occurring during atmospheric lifetime. At present, the capability of climate models in reproducing all the possible heterogeneity in aerosol optical properties represents ~~one~~ the main source of uncertainty in evaluating their DRE on climate (McComiskey et al., 2008; Stier et al., 2013). In this sense, intensive studies providing ~~with~~ the characterization of the aerosol optical properties and their local and regional variability are of great importance in order to reduce these uncertainties.

This is particularly the case of the Western Mediterranean basin. Indeed, the Mediterranean is a very complex region, characterized by the presence of air masses carrying aerosols of different origins and types (Gkikas et al., 2012). On its northern bound, it is limited by Europe, with a consequent frequent export of~~which makes that~~ anthropogenic pollution ~~is usually exported~~ from the continent towards the basin (Lelieveld et al., 2002; Pace et al., 2006). In particular, the Western part of the Mediterranean basin, surrounded by large coastal megacities, commercial harbours, and under the direct influence of some of the most industrialized areas of the continent (such as the Po Valley in Northern Italy or the Fos/Berre area in Southern France), is strongly affected by continental pollution outflows (Pérez et al., 2008; Pey et al., 2010; Di Biagio et al., 2015). The build-up of high pollution levels over the Western basin is particularly favoured during summer when the strong insolation enhances photochemical reactions and the stable meteorological conditions promote the stagnation of pollutants (Millan et al., 2000; Mallet et al., 2005).

98 In spite of this, the characterization of the optical properties of anthropogenic aerosols in this

99 part of the basin remains only limited to coastal and inland regions (Mallet et al., 2003, 2011,

100 2013; Lyamani et al., 2006; Estelles et al., 2007; Saha et al., 2008; Esteve et al., 2012;

101 Piazzola et al., 2012; Pandolfi et al., 2011 and 2014), or remote islands actually far from the

102 strong influence of continental outflows (Lyamani et al., 2015). Moreover, the majority of

103 these studies uses remote sensing measurements and analyse aerosol properties integrated

104 over the entire atmospheric column, without information on their vertical variability. Thus, at

105 present, we miss a detailed characterization of the optical properties of the pollution aerosol

106 over the entire region, in particular over the remote sea, and its vertical distribution.

107 To fill this gap, the international ChArMEx (Chemistry-Aerosol Mediterranean Experiment;

108 http://charmex.lsce.ipsl.fr) research program has supported in recent years two airborne

109 campaigns over the Western Mediterranean basin: TRAQA (Transport and Air QuAlity) in

110 2012 and SAFMED (Secondary Aerosol Formation in the MEDiterranean) in 2013.

111 In a recent paper, Di Biagio et al. (2015) have presented in situ measurements of the aerosol

112 vertical profiles acquired over the remote sea during these campaigns. Observations from

113 TRAQA and SAFMED have shown that in the Western basin pollution plumes extend as far

114 as hundreds of km from the coastline and reach up to ~4000 m, presenting a complex

115 stratified structure, and pollution plumes show a large heterogeneity in terms of composition,

116 origin, and lifetime.

117 Following these observations, we may ask: does the heterogeneity in pollution plume

118 composition, origin, and lifetime as observed in Di Biagio et al. (2015) induce heterogeneity

119 on the optical properties (in particular the single scattering albedo) of pollution aerosols in

120 this part of the basin? And, if observed, does this heterogeneity on the optical properties

121 influence the aerosol DRE? Is it necessary to take it into account to better evaluate the aerosol

122 radiative impact in the Western Mediterranean?

123 With the aim of answering these questions, in this paper we analyse data of the optical

124 properties (spectral scattering and absorption coefficients, ~~and~~ single scattering albedo) and

125 size distributions of pollution aerosols measured over the Western Mediterranean basin

126 during TRAQA. SAFMED observations have been excluded here given that only limited data

127 on the aerosol optical properties ~~are~~ were available from this campaign. The objective of the

128 paper is twofold: to provide a new dataset of aerosol single scattering albedo values which

129 can be representative of the polluted aerosols over the Western basin, and investigate the

130 sensitivity of the aerosol direct DRE to the variability of this parameter.

131

132

133

134 **2. Overview of flights during the TRAQA campaign**

135 The TRAQA campaign took place in the period 20 June – 13 July 2012. Instruments were

136 installed on board the SAFIRE (Service des Avions Français Instruments pour la Recherche

137 en Environnement, http://www.safire.fr/) tropospheric aircraft ATR-42, based in Toulouse

138 (43° 36' N, 1° 26' E, France). A total of seventeen flights, most often two flights per day,

139 with intermediate stops in different airports in southern France and Corsica, were performed

140 (flight numbers V16 to V32). The majority of flights were over the sea, with some exceptions

141 investigating inland areas in southern France. The flight altitude for the ATR-42 ranged

142 between a minimum of ~60 m to a maximum of ~5000 m above sea level (a.s.l.), and the

143 maximum flight time was 4 h. The general flight strategy consisted of legs at constant altitude

144 to sound the vertical structure by lidar observations, vertical ascents/descents to describe the

145 vertical atmospheric column and identify the main aerosol plumes, followed by straight

146 levelled runs (SLRs) within the detected aerosol layers. In the present study we will

147 exclusively consider measurements acquired during SLRs, since only during these phases the

148 whole set of aerosol optical properties (scattering and absorption coefficients) were

149 measured. A total of 21 SLRs were performed over the sea surface or inland close to the

150 coastline and will be considered in this study. Figure 1 and Table 1 summarise the

151 geographical location, date, time, and altitude of these 21 SLRs. As indicated in Table 1 each

152 SLR was about 15-20 min long. At the cruise speed of the ATR (93 ms^{-1}), this integration

153 time corresponds to about 100 km.

154

155 **3. Measurements and methods**

156 **3.1 Aircraft observations**

157 Aerosol sampling on the ATR-42 was performed using the AVIRAD system. AVIRAD is an

158 iso-axial and iso-kinetic inlet which samples air at a volumetric flow of ~350 L min^{-1}. The

159 50% passing efficiency of the inlet is 12 μm diameter. Various lines depart from AVIRAD to

160 connect to different instruments for the measurement of the aerosol physico-chemical and

161 optical properties. Additionally, several sensors for the measurements of the atmospheric

162 composition were installed on the ATR-42 aircraft as basic equipment. A brief description of

163 the different in situ measurements considered in this study from the AVIRAD system and the

164 ATR-42 equipment and their data analysis is reported in the following.

165 - The aerosol scattering coefficient (σ_s) at 450, 550, and 700 nm ~~has been~~was measured by a

166 3-wavelength~~s~~ integrating nephelometer (TSI Inc., model 3563, 6s resolution). The

167 nephelometer was calibrated prior the campaign by using air and CO_2 as reference gases.

168 Nephelometer measurements ~~have been~~were corrected for angular truncation and

169 Lambertian non-idealities by applying the formula by Anderson and Ogren (1998),

170 appropriated to submicron aerosols which we expected in the pollution plumes sampled

171 during the campaign. The measurement uncertainty on σ_s, calculated taking into account

172 for the photon counting, gas calibration, and angular corrections uncertainties, ~~is~~was

173 estimated to be lower than 10% at the three wavelengths. Averages of the scattering

174 coefficient ~~are~~were calculated over the different SLRs. The uncertainty on the SLR

175 average values ~~is~~was estimated as the combination of the measurement uncertainty and

176 the standard deviation along each individual run. For each SLR, the particle scattering

177 Ångström exponent (SAE) ~~has been~~was calculated as the power law fit of the measured

178 scattering coefficients versus wavelength to extrapolate the scattering coefficient at other

179 wavelengths than those of operation.

180 The nephelometer measured the scattering coefficient in dry air conditions. This is due to

181 the heating of the airflow while entering the aircraft cabin and the temperature increase in

182 the sensing volume of the instrument due to illumination. The relative humidity measured

183 during the flights inside the nephelometer cavity was <25% in more than 90% of cases,

184 with values up to ~40% occasionally observed <200 m over the sea surface.

185 - The aerosol absorption coefficient (σ_{abs}) at 370, 470, 520, 590, 660, 880, and 950 nm ~~has~~

186 ~~was~~been measured by a 7-wavelength~~s~~ aethalometer (Magee Sci., model AE31, 2min

187 resolution). The principle of operation of the aethalometer consists in measuring the

188 attenuation of light through an aerosol-laden filter compared to that of another portion of

189 the filter which is unexposed to the air flow and is used as a reference (Weingartner et al.,

190 2003). To yield the aerosol absorption coefficient, the spectral attenuation $\sigma_{ATT}(\lambda)$

191 measured by the aethalometer ~~has~~ ~~was~~been corrected following the procedure described by

192 Collaud Coen et al. (2010):

193
$$\sigma_{abs}(\lambda) = \frac{\sigma_{ATT}(\lambda) - \alpha(\lambda)\overline{\sigma_s(\lambda)}}{C_{ref}R(\lambda)} \qquad (1).$$

194 The different terms in equation 1 are: (i) $\alpha(\lambda)\overline{\sigma_s(\lambda)}$ or "scattering correction". In this work

195 $\alpha(\lambda)$ ~~has been~~was calculated with the formula by Arnott et al. (2005) and ~~varies~~ varied

196 between 0.02 and 0.07, while $\overline{\sigma_s(\lambda)}$ ~~is~~ was the average of the scattering coefficient along

197 the considered SLR extrapolated at the aethalometer wavelengths; (ii) C_{ref} or "multiple

198 scattering correction". C_{ref} ~~is~~ was set to 2.14 ± 0.21 (wavelength-independent) following

199 Weingartner et al. (2003); (iii) $R(\lambda)$ or "shadowing effect correction". $R(\lambda)$ depends on

200 the charge and absorptivity properties of the sampled aerosol and can be calculated as a

201 function of the particle single scattering albedo (ω). In this study, because of the absence

202 of an independent determination of ω, we used an estimated "first-guess" single scattering

203 albedo (ω^*) to calculate R. This ~~has been~~was determined as the ratio of the measured

204 scattering (σ_s) to extinction ($\sigma_s + \sigma^*_{abs}$) coefficients, with σ^*_{abs} corrected for the scattering

205 and the multiple scattering corrections, but not for the shadowing effect. The obtained

206 $R(\lambda)$ ~~varies~~ varied between 0.75 and 1 for ω^* between 0.75-0.99 at 370 nm and 0.70-0.99

207 at 950 nm. The whole uncertainty on the absorption coefficient ~~has been~~was estimated

208 with the propagation error formula taking into account for the different factors in Eq. (1)

209 and ~~varies~~ varied between 11-36% at 370 nm and 12-70% at 950 nm.

210 It has to be noticed that an enhanced absorption at single wavelengths ~~has been~~was

211 observed in several cases for the aethalometer. This ~~is~~ was possibly due to the absorption

212 on the exposed filter of gases or volatile compounds absorbing at some of the instrument

213 operating wavelengths (Weingartner et al., 2003). These anomalous points ~~have been~~were

214 accurately selected and screened from the dataset. As a result of this screening, data in

215 correspondence of only 60% of the considered SLRs ~~are~~ were available for aerosols

216 analyses.

217 The measured aerosol scattering and absorption coefficients ~~have been~~were used to

218 calculate the particle spectral single scattering albedo ~~(ω)~~ between 370 and 950 nm as:

219
$$\omega(\lambda) = \frac{\sigma_s(\lambda)}{\sigma_s(\lambda) + \sigma_{abs}(\lambda)} \qquad (2).$$

220 The uncertainty on ω ~~has~~ was~~been~~ calculated with the propagation error formula and

221 ~~varies~~ varied between 0.02 and 0.04 at all wavelengths.

222 Additionally, for each SLR for which aethalometer data ~~are~~ were available, the particle

223 absorption Ångström exponent (AAE) ~~has been~~was calculated as the power law fit of the

224 measured absorption coefficients versus wavelength.

225   -   The aerosol number size distribution (dN/dlogD_g) ~~has been~~was measured by two different

226   optical particle spectrometers: the passive cavity aerosol spectrometer probe (PCASP,

227   model 100-X, 1-s resolution, 31 size classes between 0.1 and 3.0 μm diameter, operating

228   wavelength 632.8 nm), and the optical particle spectrometer ~~SkyGRIMM~~ GRIMM

229   (GRIMM Inc., model 1.129, 6-s resolution, 32 size classes between 0.3 and 32 μm

230   diameter, operating wavelength 655 nm). For both the PCASP and the

231   ~~SkyGRIMM~~GRIMM, the measured sphere-equivalent optical diameter ~~has been~~was

232   converted in a sphere-equivalent geometrical diameter (D_g) by taking into account the

233   complex refractive index of the sampled aerosol (Liu and Daum, 2000). Differently from

234   Di Biagio et al. (2015), where the complex refractive index used to correct the size was

235   fixed based on literature values (n=1.52÷1.70, k=0.01 for pollution aerosols in the

236   Mediterranean), here the ~~Calculation are performed by fixing the imaginary part of the~~

237   ~~refractive index at 0.01, thus representing a medium absorbing aerosol, while varying the~~

238   ~~real part between 1.50 and 1.72, following the range of variability found in the literature~~

239   ~~for pollution aerosols in the Mediterranean (see Di Biagio et al., 2015 for further details).~~

240   complex refractive index to correct the size was iteratively adjusted based on optical

241   closure calculations. Full details of the procedure are provided in Sect. 3.2. ~~D_g is then set~~

242   ~~at the mean ± one standard deviation of the values obtained for the different n. A~~After

243   optical closure and refractive index correction the D_g range~~s~~ varied between 0.10-4.24 and

244   0.10-4.84 μm for the PCASP and 0.26-58.75 and 0.30-73.60 μm for the

245   ~~SkyGRIMM~~GRIMM as a function of the assumed aerosol refractive index ~~become 0.10-~~

246   ~~4.47 and 0.28-65.80 μm,~~. The uncertainty on D_g ~~with an uncertainty~~is between 1 and

247   25%. For comparison, the D_g values obtained in Di Biagio et al. (2015) were 0.10-4.47

248   and 0.28-65.80 μm for the PCASP and the GRIMM, respectively. The smallest and the

249   largest size bins of both instruments, for which the minimum and maximum edges

250   respectively are not defined, ~~have been~~were excluded from the datasets, thus reducing the

251   PCASP and GRIMM D_g ranges to 0.10-3.94 and 0.11-4.53 μm for the PCASP and 0.28-

252   50.01 and 0.34-63.03 μm for the GRIMM.~~, thus reducing the PCASP and SkyGRIMM D_g~~

253   ~~ranges to 0.11-4.17 μm and 0.31-56.21 μm, respectively.~~

254   Corrected data from the PCASP and the ~~SkyGRIMM~~GRIMM ~~are~~ were then merged to

255   obtain the aerosol size distribution over a larger size range. The two instruments

256   superimpose in a large interval covering the diameter range ~0.3~~01~~ -4.~~17~~0 μm. In this

257   interval the PCASP and the GRIMM show~~ed~~ a good agreement below 0.4 μm and above

258 1.0 μm (less than ~10% difference), while significant differences ~~we~~are observed in the

259 0.4-1.0 μm range where the PCASP underestimates the ~~SkyGRIMM~~GRIMM

260 measurements by more than ~50%. This difference is of great relevance in terms of optical

261 properties because particles in the 0.4-1.0 μm size interval are very efficient for interaction

262 with shortwave radiation. With the aim of understanding which of the two instruments

263 measures correctly in the 0.4-1.0 μm range we ~~have~~ performed an optical test, which

264 consisted in calculating with Mie theory the scattering coefficient at 450, 550, and 700 nm

265 based on the PCASP and ~~SkyGRIMM~~GRIMM size data, and then in comparing it with

266 simultaneous nephelometer measurements. Optical calculations ~~have been~~were performed

267 by fixing the complex refractive index at 1.6-0.01i, so at the mean of the range of values

268 reported in the literature for pollution aerosols (Ebert et al., 2002 and 2004; Mallet et al.,

269 2003 and 2011; Müller et al., 2002; Raut and Chazette, 2008). SLRs characterized by a

270 low variability in terms of scattering coefficient and particle concentration ~~have been~~were

271 selected. The results of the optical test indicate that in the 0.4-1.0 μm range the size

272 distribution of the ~~SkyGRIMM~~GRIMM is more accurate since it permits to most closely

273 reproduce nephelometer observations (<5% mean difference between calculations and

274 observations at the three wavelengths, compared to differences up to 15-21% if PCASP

275 data are used in the 0.4-1.0 μm size range). Thus, a combined PCASP-

276 ~~SkyGRIMM~~GRIMM number size distribution $dN/dlogD_g$ in the ~~~~~0.1~~10~~ to 5~~0.01-~~

277 ~~63.03~~36.21 μm diameter range ~~has been~~was ~~calculated~~ estimated by considering PCASP

278 data up to 0.~~31~~30 μm and ~~SkyGRIMM~~GRIMM data above. ~~Together with the number~~

279 ~~size distribution, for each SLR also t~~The volume size distribution was also computed as

280 $dV/dlogD_g=\pi/6\,D_g^3\,dN/dlogD_g$ ~~has been calculated~~. Averages of the number and volume

281 size distributions over each SLRs were calculated.

282 Nonetheless, due to a technical problem, ~~SkyGRIMM~~GRIMM data were only available

283 below ~350 m (~970 hPa).

284 - The total particle number concentrations in the ~~Aitken~~ultrafine mode (4 nm-0.1 μm;

285 ~~dN_{Aitken}~~dN_{UFP}, i.e. formerly defined as Aitken mode in Di Biagio et al., 2015) and

286 accumulation mode (0.1-1.0 μm; dN_{Acc}) ~~modes have been~~were calculated by combining

287 condensation particle counter measurements of particle concentration in the 0.004 – 3 μm

288 range (CPC, TSI Inc., model 3775, 5-s resolution) and size distribution data. Due to the

289 fact that above 350 m the ~~SkyGRIMM~~GRIMM ~~is~~was not available, only PCASP data ~~are~~

290 were used in the calculations of $dN_{\text{Aitken}UFP}$ and dN_{Acc} over the whole altitude range.

dN$_{\text{AitkenUFP}}$ is was estimated as the difference between CPC concentration and the integral of PCASP data between 0.1 and 3.0 µm, while dN$_{\text{Acc}}$ is was obtained by integrating the PCASP number concentrations in the 0.1-1.0 µm interval. The underestimation of the PCASP number concentration between 0.4 and 1.0 µm, as discussed above, is was estimated to induce a ~20% underestimation of the dN$_{\text{Acc}}$ calculated here, whilst it has had almost a negligible impact on dN$_{\text{AitkenUFP}}$. The dN$_{\text{UFP}}$ and dN$_{\text{Acc}}$ and dN$_{\text{Aitken}}$ obtained in correspondence of each SLR have been were used to calculate the Aitken ultrafine-to-accumulation ratio dN$_{\text{AitkenUFP}}$/dN$_{\text{Acc}}$.

- The carbon monoxide (CO) and ozone (O$_3$) mixing ratios have been were measured by the MOZART instrument (CO, 30-s resolution and ±5% nominal uncertainty, O$_3$, 4-s resolution and ±2% nominal uncertainty) (Nedelec et al., 2003). Starting from the measured O$_3$ and CO, the ozone enhancement ratio (ΔO$_3$/ΔCO) hwas been calculated, i.e. the ratio of the ozone to carbon monoxide variations compared to their baseline values. A background value of ~70 ppbv in the boundary layer and ~60 ppbv in the free troposphere has been was used for CO, while the background has been was set at ~30 ppbv for O$_3$ at all levels (Di Biagio et al., 2015). ΔO$_3$/ΔCO data have been were used together with dN$_{\text{AitkenUFP}}$/dN$_{\text{Acc}}$ to retrieve information on the age of the sampled air masses, as discussed in Di Biagio et al. (2015).

In order to compare SLRs measurements obtained at different altitudes, the data analysed here are were reported to standard temperature and pressure (STP) using T=293.15 K and P=1013.25 hPa. In this case, the scattering and absorption coefficients are were scaled to STP conditions and the particle concentrations (in number or volume) are were given as particles per standard cm^{-3} (scm^{-3}). Where not explicitly indicated, data refer to STP conditions.

In Table 2 we summarize main information and uncertainties for the different aerosol instruments considered in this study.

3.2 Optical closure and estimation of the aerosol complex refractive index

An optical closure study was realised to estimate the complex refractive index (m=n-ik) of pollution aerosols based on optical and size data. The flowchart of the procedure is illustrated in Fig. 2. Optical closure consisted in recalculating the spectral scattering σ$_s$ and absorption σ$_{\text{abs}}$ coefficients measured for each SLR by using the measured size distribution as input and by varying the real (n) and imaginary (k) parts of the complex refractive index in the calculations. Then, n and k were fixed when the best agreement between measurements and

calculations was found. Given that the size distribution measured by the PCASP and the GRIMM depends on the aerosol refractive index, the optical-to-geometrical diameter conversion was recalculated at each iteration based on the assumed n and k. Optical calculations were performed using Mie theory for spherical particles. The Mie_single.pro IDL routine available at http://www.atm.ox.ac.uk/code/mie/mie_single.html was used. In the calculations the real part of the refractive index was varied in the range 1.30-1.80 at steps of 0.01, while the imaginary part in the range 0.001-0.1 at steps of 0.001, for a total of 5100 inversions for each SLR dataset. The uncertainty on the real and imaginary parts of the refractive index was estimated with a sensitivity study. To this purpose, the values of n and k were also obtained by using as input the observed σ_s, σ_{abs}, and $\dfrac{dN}{d\log D_g}$ plus or minus one standard deviation on their measurement. The deviations of the values of n and k retrieved in the sensitivity study with respect to those obtained in the first inversions were assumed to correspond to the one standard deviation uncertainty. The estimated uncertainty was <5% for n and ~25-30% for k.

3.2 3 Boundary layer height estimation

The planetary boundary layer (BL) top height has beenwas estimated from meteorological observations (temperature, T, potential temperature, θ, and relative humidity, RH) for each vertical sounding performed during TRAQA flights (see Di Biagio et al., 2015). The boundary layer top height is was between 730 and 1500 m, with an average of ~1000 m. The location of each SLR, so if it is within the boundary layer or in the free troposphere, has beenwas determined based on the planetary boundary layer top height estimated from the closest vertical sounding performed during each flight.

3.3 4 Tracking the origin of the sampled air masses

As discussed in Di Biagio et al. (2015), aerosol observations during TRAQA were mostly influenced by pollution/anthropogenic particles exported from different sources around the basin (Northern Italy/Po Valley, Southern France, Barcelona area). The Lagrangian trajectory model FLEXPART (FLEXible PARTicle dispersion model, Stohl et al., 1998), adapted for

the WRF (Weather Research and Forecasting) meteorological input (Brioude et ~~al.~~, 2013) ~~has been~~was used here to track the origin of air masses sampled during SLRs. Five-day three-dimensional back-trajectories ~~have been~~were calculated using the WRF meteorological output at a 30 km horizontal resolution and 28 vertical model levels up to 50 hPa. The model specific humidity and potential vorticity ~~is~~were also interpolated along the trajectory path. Based on FLEXPART simulations, data for the different SLRs ~~have been~~were separated as a function of the origin of the sampled air masses. Three different sectors ~~have been~~were defined: the Western sector, which includes trajectories coming from the Atlantic Ocean and travelling over France or northern Spain before reaching the Western basin; the Eastern sector, including air mass trajectories from continental Europe that have travelled over northern Italy-Po Valley before entering the basin; and the Open sea sector, which consists of trajectories coming from the Western or Eastern sectors which have experienced at least 2 days of subsidence over the sea in the Western basin and thus can be taken as representative of the regional background aerosol or local pollution sources, i.e. ship emissions. The three different selected ~~Sectors~~ sectors are shown in Fig. 1, while Table 1 also reports the identified ~~Sector~~ sector of origin for the air masses sampled during the different SLRs.

~~-~~As discussed in Di Biagio et al. (2015), several flights were affected by dust particles exported over the basin from Northern Africa. SLRs data dominated by dust ~~have been~~were identified based on the combined analysis of back-trajectories, lidar profiles and optical data, and ~~have been~~were excluded from the dataset. However, for some SLRs, the possible mixing of dust aerosols with pollution particles cannot be a priori excluded.

3.~~4~~5 Radiative model calculations

Radiative transfer calculations ~~have been~~were performed to estimate the instantaneous aerosol direct radiative effect in the shortwave spectral range for different cases and in clear-sky conditions. The objective of the calculations ~~is~~was to test the sensitivity of the DRE to the variability of the aerosol optical properties, in particular the single scattering albedo, as observed in this study. The GAME radiative transfer model (Dubuisson et al., 1996 and 2006) ~~has been~~was used in this study to compute the vertical profiles of downward and upward shortwave irradiances over the 0.28-3.0 μm spectral range. The model calculates radiances and irradiances at various atmospheric levels at 400 cm^{-1} spectral resolution between 0.28 and 0.5 μm, and 100 cm^{-1} resolution between 0.5 and 3 μm. Spectral absorption by principal atmospheric gases (H_2O, CO_2, O_3, CH_4, N_2O, O_2) is taken into account in the

model. The discrete ordinate method (Stamnes et al., 1988) with twelve streams ~~i~~was used in the simulations to describe multiple scattering. Simulations ~~have been~~were performed with and without aerosols by fixing the solar zenith angle (θ) at 60°, i.e. at about the mean of the diurnal value at the latitudes of north-Western Mediterranean, and for a mid-latitude climatological summer meteorological profile. The aerosol optical properties that are used as input in the GAME radiative code are the spectral variation of the optical depth (τ), the asymmetry parameter (g) and the single scattering albedo (ω). The difference of the net shortwave fluxes (downward minus upward irradiances) with and without aerosols at the surface and at TOA ~~i~~was used to estimate the aerosol DRE at these two levels. The atmospheric DRE ~~i~~was then calculated as the difference between the TOA and the surface values. Finally, the ratio of the DRE to the aerosol optical depth at 500 nm, i.e. the aerosol forcing efficiency (FE), ~~i~~was obtained. The shortwave heating rate at the altitude z ~~i~~was also calculated as:

$$\frac{\partial T}{\partial t} = -\frac{1}{\rho C_p}\frac{\partial F(z)}{\partial z} \quad (3)$$

where T is the air temperature, ρ is the air density, C_p is the specific heat of the air, and F(z) is the net flux at the altitude z.

4. Results

4.1 Overview over the different SLRs

Figure ~~2~~ 3 shows the averages altitude, spectral scattering (σ_s) and absorption (σ_{abs}) coefficients, scattering and absorption Ångström exponent (SAE and AAE, respectively), ozone enhancement factor ($\Delta O_3/\Delta CO$), and ~~Aitken~~ultrafine-to-accumulation particle ratio ($dN_{\text{~~Aitken~~UFP}}/dN_{Acc}$) measured for the different SLRs during TRAQA.

As shown in Fig. ~~2~~ 3 and Table 1, the large majority of the SLRs were performed within the boundary layer at an altitude <1000 m. Only four SLRs (V25_R2, V25_R3, V26_R1, and V30_R1) measured aerosols in the free troposphere between 1800 and 3500 m. The sampled aerosols originated in each of the three different source sectors identified based on FLEXPART back-trajectories (Western, Easter~~n~~, and Open ~~s~~Sea), with a larger number of cases from the Western sector compared to the Eastern and the Open ~~Sea~~ sea areas.

For all the different cases, the measured scattering coefficient was in the range 16-73 Mm^{-1} at 450 nm and 8-30 Mm^{-1} at 700 nm. The absorption coefficient was generally below 10 Mm^{-1} at all wavelengths, with the exception of V27_R1 and V32_R1 for which values up to ~20 Mm^{-1} at 370 nm were measured. For these two cases also the highest values of the particle concentration in the accumulation mode (~1700-2200 # cm^{-3}, not shown) and among the highest values of the scattering coefficient were measured. For all cases, both σ_s and σ_{abs} decrease with the wavelength. The pronounced spectral variability of σ_s, in particular, indicates the dominance of pollution/anthropogenic fine particles in the sampled plumes.

The SAE varied between 0.96 and 1.94, while the AAE varied between 0.92 and 1.65, with an average of ~1.20. The AAE was not calculated for few cases with very low values of the absorption coefficient (σ_{abs} at 370 nm < 1.5 Mm^{-1}). Both the SAE and the AAE obtained in this study fall in the range of variability indicated by several authors to identify pollution/anthropogenic aerosols or pollution mixed with other aerosol types in the Mediterranean basin (SAE>1-1.5, and AAE~1-1.5; Pace et al., 2006; Toledano et al., 2007; Mallet et al., 2013). Values of AAE larger than unity, in particular, might suggest the possible mixing of pollution with brown carbon or dust particles over the basin (Russell et al., 2010; Mallet et al., 2013).

For all the measured SLRs the $\Delta O_3/\Delta CO$ and the dN_{UFP}/dN_{Acc} ratios varied in the range 0.37-1.02 and 1-50, respectively, for O_3 and CO varying between 24-78 and 69-136 ppbv and dN_{UFP} and dN_{Acc} between 320-22500 and 100-2170 # cm^{-3}. $\Delta O_3/\Delta CO$ and the dN_{UFP}/dN_{Acc} are linked to the photochemical (rate of ozone formation) and physical (rate of ultrafine to accumulation particle conversion) processes responsible for the aging of the aerosol plumes. The range of measured values here includes both cases with high dN_{UFP}/dN_{Acc} and low $\Delta O_3/\Delta CO$, typical of fresh plumes, and cases with low dN_{UFP}/dN_{Acc} and high $\Delta O_3/\Delta CO$, indicative of more aged air masses (Di Biagio et al., 2015).

The summary of observations from Fig. 3 suggests that the set of SLRs measurements considered in this study can be considered representative of a wide range of different atmospheric conditions occurring over the basin both in terms of sources, loadings, and lifetime for pollution aerosols.

4.2 Particle size distributions

Figure 3 4 shows the mean and the range of variability of the number and volume size distributions measured during horizontal SLRs within pollution layers during TRAQA. Data were separated based on the origin of the sampled air masses and refers only to cases at <350 m altitude within the boundary layer. The absolute uncertainty on the measured concentration, as also reported in Table 2, is ~15% for particle diameters below 0.31 µm and ~10% at larger sizes. The grey shading indicates considerable variability in the number concentration of the size distributions, of approximately one order of magnitude for much of the size range measured. This reflects the relative wide range of aerosol loadings encountered during the campaign. The minimum of the size distribution over the whole diameter range was measured in the Western sector (V32_R3), whilst the largest number concentrations in the super-micron range were observed in correspondence of V19_R1 and V32_R1. For all the other SLRs, the size distributions were very similar, especially at diameters below ~5 µm.

The measured number size distribution from each SLR has been was fitted with multi-mode lognormal functions:

$$\frac{dN}{d\log D_g} = \sum_i \frac{N_{tot,i}}{\sqrt{2\pi}\log\sigma_{g,i}} \left(-\frac{\left(\log D_p - \log D_{g,i}\right)^2}{2\log^2\sigma_{g,i}} \right) \qquad (4).$$

For each mode ii, N_{tot} represents the total aerosol number concentration, D_g the median diameter, and σ_g the geometric standard deviation. The logarithm refers to base 10. Size data were fitted automatically using the MPCURVEFIT IDL routine available at http://www.physics.wisc.edu/~craigm/idl/fitting.html. Since the aim of the fitting is to describe as closely as possible the measured number size distributions for subsequent optical calculations (Sect. 4.4), up to seven modes were used to fit the data. The correlation coefficient for the fit functions was larger than 0.97 for all cases. The parameters of the lognormal fits are reported in Table 3. The first mode of the size distribution is generally at 0.13-0.14 µm, whilst the largest mode is between ~5 and 8 µm for the different cases.

4.3 Spectral single scattering albedo: variability as a function of air mass origin and height

Figure 4 5 shows the spectral ω for the different SLRs considered in this study. Data have been were separated based on the origin of the sampled air masses. The single scattering albedo varies in the range 0.84-0.98 at 370 nm and 0.70-0.99 at 950 nm and generally decreases with the wavelength, as it is typical for pollution particles (Dubovik et al., 2002).

Only in two cases (V19_R1 and V30_R2) the single scattering albedo increases with wavelength. For these cases also very high values of ω ~~are~~ were observed (0.92-0.97 for V19_R1 and 0.98-1.0 for ~~V32~~V30_R2), which may suggest the possible mixing of pollution with sea spray or desert dust particles, both showing low absorption in the shortwave range (Bergstrom et al., 2007). The lowest values of the single scattering albedo ~~are~~ were measured for V27_R1 (0.84-0.70 between 370 and 950 nm) sampled at ~160 m and originated in the Open Sea sector. Data in Fig. ~~2~~ 3 also indicate for V27_R1 very low values of $\Delta O_3/\Delta CO$ (~0.37) and a relatively high $dN_{\text{AitkenUFP}}/dN_{Acc}$ (~7), which suggests that V27_R1 ~~is~~ was a fresh plume possibly associated to local emissions, i.e. ship plumes, over the basin. If we exclude V27_R1, the range of measured values appears comparable (within error bars) for the three considered sectors (Western, Eastern, and Open sea; ω between 0.88 and 0.98 at 370 nm and 0.83 and 0.99 at 950 nm).

The vertical variability of ω, together with $dN_{\text{AitkenUFP}}/dN_{Acc}$, $\Delta O_3/\Delta CO$, SAE, and AAE, is shown in Fig. ~~5~~ 6 for the different considered cases. With the only exception of V27_R1, for which the lowest values ~~are~~ were observed below 200 m, the single scattering albedo does not show a clear trend with height, with a similar range of values measured in the boundary layer, below ~1000 m, and in the free troposphere up to ~3500 m. As for ω, the AAE does not significantly vary with height. At the same time, $dN_{\text{AitkenUFP}}/dN_{Acc}$ and SAE decrease with height, with a concurrent slight $\Delta O_3/\Delta CO$ increase, which may suggest an increase of plume age with height. The ensemble of these observations seems to indicate that, for our observed cases, the absorptivity properties of the sampled plumes do not depend on the altitude and associated air mass age of the plume. It should be pointed out, however, that the majority of cases considered here ~~have been~~were sampled below 1000 m, so in the boundary layer, and the statistics in the free troposphere is only limited to a few events.

Values of the single scattering albedo measured in this study are comparable with values reported at several other sites in the Central and Western Mediterranean region for pollution aerosols (Mallet et al., 2003 and 2013; Meloni et al., 2006; Saha et al., 2008; Di Biagio et al., 2009; Pandolfi et al., 2011). The single scattering albedo from these studies ~~is observed to varies~~y in the range 0.84-0.95 at 440 nm, 0.76-0.98 at 500-550 nm, and 0.80-0.87 at 870 nm. Compared with the literature, larger and lower values are obtained in the present study for few cases mostly influenced by sea spray, desert dust, and local fresh emissions, respectively.

4.4 ~~COptical closure and estimation of the aerosol c~~omplex refractive index _of pollution aerosols_

As discussed in the previous section, the single scattering albedo of pollution aerosols shows a relatively large variability. Here we investigate the impact of this variability on the complex refractive index ($m=n-ik$) of the particles.

For eight selected SLRs for which both complete optical (scattering and absorption coefficients, and single scattering albedo) and size distribution measurements were available, the aerosol spectral complex refractive index ~~has been~~was estimated by optical closure study _as described in Sect. 3.2_. These cases correspond to V19_R1, V21_R1, V21_R3, V23_R2, V27_R1, V31_R1, V32_R1, V32_R3 sampled within the boundary layer at <350 m altitude.

The comparison of the measured and ~~calculat~~modelled σ_s and σ_{abs} are shown in Fig. ~~6~~7, while the retrieved real and imaginary parts of the refractive index for the different SLRs are reported in Fig. ~~7~~8. Data in Fig. ~~7~~8 are also compared to the real and imaginary parts of the refractive index for the single components (insoluble, water soluble, soot, and sea salt) considered in the OPAC model (Optical Properties of Aerosols and Clouds, Hess et al., 1998) to represent continental, urban and maritime polluted aerosols.

As shown in Fig. ~~6~~7, a very good agreement ~~is~~ was found between the calculated and the measured scattering and absorption coefficients, with an average difference of less than 5% for both σ_s and σ_{abs}. For our analysed cases n and k vary in the range 1.67-1.75 and 0.~~003~~004-0.0~~38~~50 at 370 nm and 1.41-1.~~75~~77 and 0.002-0.0~~68~~897 at 950 nm, respectively. The imaginary part of the refractive index slightly increases with wavelength, while ~~a~~not a clear tendency is found for the~~decrease is observed for the~~ real part~~in most cases~~, which in some of the cases increases with wavelength and in others decreases. Highest values of k are obtained for V27_R1, which also shows the absolute lowest values of ω in our dataset (0.84-0.70), followed by V32_R1 and V32_~~R2~~R3, which also present relatively low values of ω (0.~~95~~92-0.83). The lowest k, as well as among the lowest n, is instead obtained for V19_R1 (ω=0.92-0.96). The comparison of our data with OPAC values for single components suggests that in most cases particles are composed of a mixing of insoluble and water soluble components, with possible contributions of soot (V27_R1) ad sea salt (V19_R1).

~~-~~The results of the complex refractive index obtained in this study are in agreement with previous estimates obtained for pollution aerosols in continental Europe (n~1.50-1.72 and k~0.001-0.1 for UV-visible wavelengths e.g. Ebert et al., 2002, 2004; Müller et al., 2002; Mallet et al., 2003, 2011; Raut and Chazette, 2008). Larger values of both n and k are instead

obtained here compared to AERONET retrievals at different sites in the Western Mediterranean (1.38-1.46 for n and 0.003-0.01 for k at 440 and 670 nm; Mallet et al., 2013).

Figure 8 9 shows the results of the correlation analysis between the single scattering albedo and the complex refractive index obtained for the analysed cases. For the real part, the range of retrieved n values is larger (1.41-1.7074) for ω greater than ~0.95, while as the single scattering albedo decreases the real part converges to ~1.7065-1.75 at all wavelengths. A strong correlation is observed between ω and k at all wavelengths, that is the lower the single scattering albedo, the higher the imaginary part. A linear regression fit was applied to the ω-k datasets at the seven wavelengths (R^2=0.83-0.95 at all wavelengths for the different fits). The slope of the fit varies between -2.2 and -6.9, and decreases with the wavelength (in particular if the outlier points of k in correspondence of V27_R1 are eliminated), in agreement with the decrease of ω with λ for pollution aerosols. TThe intercept for all cases is lower than 1 (0.934-0.97), with lowest values (0.94) obtained at 880 and 950 nm. This is possibly associated to a slight underestimation of ω which, especially at these wavelengths, is difficult to determine given the high uncertainty on the particle absorption coefficient. Another source of uncertainty is the size distribution, which influences the results of Mie calculations, and thus has a direct impact on the refractive index retrieval.

4.5 Influence of the single scattering albedo variability on the aerosol direct shortwave radiative effect (DRE)

Radiative transfer model calculations with the GAME model have beenwere performed with the aim of investigating the impact of the variable optical properties, and in particular the single scattering albedo, on the shortwave direct radiative effect of pollution particles in the Western Mediterranean basin.

Simulations have beenwere performed by considering three different vertical aerosol profiles, based on observations reported by Di Biagio et al. (2015): i. aerosols only confined in the BL (whose altitude is fixed at 1000 m, in the mean of observations during TRAQA); ii. 50% of the aerosol optical depth in the BL and 50% in the FT (which is considered to extend between 1000 and 4000 m); iii. 20% of the aerosol optical depth in the BL and 80% in the FT. For the different cases we fixed the total aerosol optical depth at 0.2 at 550 nm, which corresponds to the mean of observations obtained over the Western basin during TRAQA (Di Biagio et al., 2015). However, results will be given as FE, so they are independent on the chosen optical depth. We assumed a uniform aerosol distribution and constant optical properties within the

BL and the FT for the three different considered profiles. This assumption ~~co~~omes from the observations of the present study, which do not evidence any significant change of the aerosol properties with height. Aerosol spectral optical properties, both in the BL and in the FT up to 4000 m, ~~are~~ were assumed from observations, as explained in the following.

The GAME model requires as input the aerosol optical depth, single scattering albedo, and asymmetry factor at 7 wavelengths between 330 and 1500 nm. The spectral optical depth between 330 and 1500 nm wa~~i~~s extrapolated from the fixed value of 0.2 at 550 nm by assuming a Ångström exponent of 1.5, in the mean of our observations for pollution aerosols (see Fig. 2). For the single scattering albedo, we considered 3 different sets of values which correspond to the minimum, maximum, and mean of the values observed in this study (the absolute minimum for V27_R1 ~~has been~~was excluded for calculations since it represents an outlier in our data). The ω values at 370-950 nm as obtained from experimental data ~~are~~ were then extrapolated at the 7 GAME wavelengths (Table 4). The asymmetry factor wa~~i~~s calculated from Mie theory based on the refractive index values and size distribution data for the eight cases considered in the previous Section. The spectral variation of g used in the radiative transfer calculations wa~~i~~s estimated as the mean of the values obtained for these eight cases extrapolated at the 7 GAME wavelengths. The obtained g varie~~s~~d between 0.60 at 330 nm and 0.51 at 1500 nm. These values are consistent with previous estimates of g obtained for pollution aerosols over the Mediterranean basin (Meloni et al., 2006; Saha et al., 2008; Mallet et al., 2011).

Background stratospheric aerosols (above 12 km) ~~are~~ were also taken into account for radiative calculations; optical properties from the OPAC stratospheric aerosol model (Hess et al., 1998) ~~a~~were assumed.

Finally, in addition to aerosol optical properties, the GAME model requires as input the albedo of the surface (A_S) at 5 wavelengths between 448 nm and 2130 nm. In this study, simulations ~~are~~ were performed over the sea surface. The albedo of the sea surface ~~is~~ was obtained from Jin et al. (2004), which provide a parameterisation of A_S as a function of chlorophyll concentration (Chl), wind speed (w), aerosol optical depth at 500 nm (τ), and the solar zenith angle (θ). For this study A_S ~~is~~ was estimated for Chl=0, w=6-9 m s^{-1}, τ=0.24 (extrapolated from the value of 0.2 at 550 nm), and θ=60°, and it ~~varies~~ varied between 0.009 and 0.005 in the considered 448-2130 nm spectral range.

Results of the radiative transfer simulations are shown in Fig. ~~9~~10, which reports the FE at the surface, TOA, and atmosphere (FE$_S$, FE$_{TOA}$ and FE$_{ATM}$) for the maximum, mean, and

613   minimum of the single scattering albedo observed in this study. Results of the simulations are
614   mostly independent on the vertical distribution of the aerosols (less than ~5% changes for
615   FE_S, FE_{ATM}, and FE_{TOA} for the three different profiles used in the simulations), so the mean
616   of the results obtained for the three cases is reported in Fig. 910. The forcing efficiency varies
617   between -160 and -235 (FE_S), -137 and -92 (FE_{TOA}), and +23 and +143 (FE_{ATM}) W m^{-2} τ^{-1} for
618   ω varying between its maximum and minimum values. Estimates of the forcing efficiencies
619   in correspondence of the mean of ω are -198, -113, and +85 W m^{-2} τ^{-1} at the surface, TOA,
620   and atmosphere, respectively. The corresponding instantaneous shortwave heating rate at the
621   surface varies between 0.2 and 2.0 K day^{-1} for ω between its maximum and minimum.
622   As expected, the lower the single scattering albedo, the larger in absolute value the FE_S and
623   FE_{ATM} and the lower the FE_{TOA}. This is due to the impact of absorption on the amount of
624   radiation trapped in the atmosphere and transmitted towards the surface, which thus enhance
625   the radiative effect in the atmosphere and at the surface for decreasing ω. Conversely, the
626   larger the particle absorption, the lower the effect on the radiation reflected back to space,
627   and thus the decrease of the intensity of the cooling effect at the TOA. Changes in the single
628   scattering albedo of the particles between its maximum and minimum ($\Delta\omega$=0.1-0.2 at the
629   different wavelengths) determine about a 50% strengthening of the direct shortwave radiative
630   effect at the surface, and a reduction of ~30% the effect at the TOA. Consequently, the
631   atmospheric FE may vary up to an order of magnitude. These results thus highlight the
632   sensitivity of the DRE on the absorptivity properties of the particles, as well as the
633   importance of accurately reproducing the single scattering albedo of aerosols to correctly
634   evaluate their direct radiative effect.
635   The results of the present study are in quite good agreement with previous estimates of the
636   aerosol forcing efficiency for pollution aerosols in the Mediterranean area. FE_S, FE_{ATM}, and
637   FE_{TOA} obtained here compare well with data obtained in the Central Mediterranean by Di
638   Biagio et al. (2009, 2010), who provide estimates based only on observational data, i.e.
639   without any assumption on the aerosol optical properties. In these studies they report a
640   forcing efficiency of ~-200 and -164 W m^{-2} τ^{-1} at the surface and TOA at solar zenith angles
641   of 50°-60° for mixed aerosols (pollution plus sea salt particles). They estimate an increase in
642   absolute value of FE_S of about 20-40% due to a decrease of 0.1-0.2 of the single scattering
643   albedo (at 415 and 868 nm) of the aerosols, as well as a concurrent increase of FE_{TOA} of
644   about 10-40%. The observations obtained in this study fall in the range of variability reported
645   by Di Biagio et al. (2009, 2010). Our data also agree with estimates of Saha et al. (2008),
646   reporting for pollution aerosols measured in the French Mediterranean coast up to 40%

variability in the FE_S and FE_{TOA}, concurrently with 70% increase of FE_{ATM}, due to a ω change of 0.15 at 525 nm. Conversely, our estimates at the surface and TOA are larger in absolute value compared to data reported for continental Europe by Horvath et al. (2002), who estimated a FE_S of ~-164 W m^{-2} τ^{-1} and a FE_{TOA} of -50 W m^{-2} τ^{-1} for polluted aerosols with ω=0.90 at 520 nm, thus comparable with our mean values of single scattering albedo for pollution aerosols.

5. Conclusions

In this study we have presented measurements of the spectral optical properties (scattering and absorption coefficients and single scattering albedo) and particle size distributions for pollution aerosols obtained over the remote sea in the Western Mediterranean basin during the TRAQA campaign in summer 2012. The set of observations analysed in this study can be assumed to be representatives of a wide range of different conditions that can be observed over the basin, both in terms of pollution sources, aerosol loadings, and lifetimes of the plumes. The detailed characterization of the spectral optical properties of pollution aerosols in the Western basin was missing to date.

Observations from the present study show a large variability of the optical properties of pollution aerosols over the basin, in particular of the spectral single scattering albedo. Values of ω in the range 0.84-0.98 at 370 nm and 0.70-0.99 at 950 nm are observed in this study. This variability of ω does not seem to be clearly linked neither to the particle origin, nor to the altitude and associated ~~ageing~~aging of the sampled plumes. The variability of ω reflects in a large variability for the complex refractive index of pollution aerosols, which is estimated to span in the range 1.41-1.75 for the real part and 0.002-0.068 for the imaginary part between 370 and 950 nm. The analysis of the complex refractive index suggests that possible differences in terms of particle compositions can explain in part the observed variability of ω. A large range of compositions has been however reported for pollution aerosols in Europe and the Mediterranean basin (Mallet et al., 2003; Ebert et al., 2004; Pey et al., 2010; Piazzola et al., 2012) and a more detailed analysis of the aerosol composition for the cases ~~obtain~~measure~~e~~d her~~ein this study~~ should be addressed.

Based on the observations of the present study, the variability of optical properties for pollution aerosols can arise from the combination of different factors, linked to the origin, production mechanism, and ~~ageing~~aging of the plumes along their lifetime, as well as the possible mixing of different plumes with different characteristics. So, the inherent

680 heterogeneity of sources, coexistence of different air masses, and multiple physical and
681 chemical processes occurring in a complex environment such as the Western Mediterranean
682 may give rise to this inherent variability of the particle single scattering albedo.

683 This observed variability on ω has a large influence on the direct shortwave radiative effect
684 of pollution aerosols at the surface, TOA, and within the atmosphere. For instance, a change
685 of up to an order of magnitude (from +23 to +143 W m^{-2} τ^{-1} at 60° solar zenith angle) in the
686 atmospheric radiative effect is estimated due to the variability of the single scattering albedo
687 within the range of values observed in this study. The change in the amount of atmospheric
688 absorbed solar radiation may have a strong impact on the temperature profile and the
689 atmospheric thermal structure, with important consequences on several processes, such as
690 cloud formation and precipitations. The strong sensitivity of the DRE also at the surface, up
691 to 50% for varying ω, on its turn, may largely impact the rate of evaporation over the basin,
692 which is also a crucial component of the hydrological cycle (Nabat et al., 2015). Given the
693 large sensitivity of the Mediterranean area and the high risk of desertification for this region
694 (Giorgi and Lionello, 2008; IPCC, 2013) any factor possibly impacting the hydrological cycle
695 should be taken carefully into account by regional climate models. In this view, results from
696 the present study can be used to provide a constraint of the absorption properties of pollution
697 particles in the Western Mediterranean basin to use in regional modelling studies.
698 Constraining these properties constitutes a crucial step in order to better assess the role of
699 aerosols on the radiative balance of this region and to ameliorate the capability of making
700 projection on future climate changes.

701

702 **Author contributions**

703 J.-L. Attié, F. Ravetta, G. Ancellet, and P. Formenti designed the TRAQA experiment and
704 coordinated the campaign. C. Gaimoz, N. Grand, and C. Di Biagio operated the instruments
705 on board the ATR-42 during the flights. C. Di Biagio performed the data analysis with
706 contributions from L. Doppler and P. Formenti. S. Bucci and F. Fierli performed the
707 FLEXPART simulations. M. Mallet and P. Dubuisson provided the GAME code for radiative
708 calculations. C. Di Biagio wrote the manuscript with contributions from all co-authors.

709

710

711

Acknowledgements

All measurement presented here are from the Chemistry-Aerosol Mediterranean Experiment project (ChArMEx, http://charmex.lsce.ipsl.fr), which is the atmospheric component of the French multidisplinary program MISTRALS (Mediterranean Integrated Studies aT Regional And Local Scales). ChArMEx-France was principally funded by INSU, ADEME, ANR, CNES, CTC (Corsica region), EU/FEDER, Météo-France, and CEA. TRAQA was funded by ADEME/PRIMEQUAL and MISTRALS/ChArMEx programmes and Observatoire Midi-Pyrénées. C. Di Biagio thanks the Centre National des Etudes Spatiales (CNES) for financial support.

The authors wish to thank the technicians, pilots and ground crew of SAFIRE (Service des Avions Francais Instruments pour la Recherche en Environnement) for facilitating the instrument integration and conducting flying operations. We thank S. Chevaillier, R. Loisil, J. Pelon, and P. Zapf for their contribution during the campaign. We also wish to thank G. Siour for his help to run the GAME radiative code. Helpful comments and suggestions by two anonymous reviewers are acknowledged.

References

Anderson, T. L. and Ogren, J. A.: Determining aerosol radiative properties using the TSI 3563 integrating nephelometer, Aerosol Sci. Technol., 29, 57–69, 1998.

Arnott, W., Hamasha, K., Moosmüller, H., Sheridan, P. J. , and Ogren, J. A.: Towards aerosol light-absorption measurements with a 7-wavelength aethalometer: Evaluation with a photoacoustic instrument and 3-wavelength nephelometer, Aerosol Sci. Tech., 39(1), 17–29, 2005.

Bergstrom, R. W., Pilewskie, P., Russell, P. B., Redemann, J., Bond, T. C., Quinn, P. K., and Sierau, B.: Spectral absorption properties of atmospheric aerosols, Atmos. Chem. Phys., 7, 5937-5943, 2007.

Boucher, O., et al., Clouds and Aerosols. Stocker, T., & Qin, D. (eds), Climate Change 2013: The Physical Science Basis. Contribution of Working Group I to the Fifth Assessment Report of the Intergovernmental Panel on Climate Change. Cambridge Univ. Press, Cambridge, United Kingdom and New York, NY, USA, 2013.

Brioude, J., Arnold, D., Stohl, A., Cassiani, M., Morton, D., Seibert, P., Angevine, W., Evan, S., Dingwell, A., Fast, J. D., Easter, R. C., Pisso, I., Burkhart, J., and Wotawa, G.: The Lagrangian particle dispersion model FLEXPART-WRF version 3.1, Geosci. Model Dev., 6, 1889-1904, doi:10.5194/gmd-6-1889-2013, 2013.

Collaud Coen, M., Weingartner, E., Apituley, A., Ceburnis, D., Fierz-Schmidhauser, R., Flentje, H., Henzing, J. S., Jennings, S. G., Moerman, M., Petzold, A., Schmid, O., and Baltensperger, U.: Minimizing light absorption measurement artifacts of the Aethalometer: evaluation of five correction algorithms, Atmos. Meas. Tech., 3, 457–474, doi:10.5194/amt-3-457-2010, 2010.

Di Biagio, C., di Sarra, A., Meloni, D., Monteleone, F., Piacentino, S., and Sferlazzo, D.: Measurements of Mediterranean aerosol radiative forcing and influence of the single scattering albedo, J. Geophys. Res., 114, D06211, doi:10.1029/2008JD011037, 2009.

752 Di Biagio, C., di Sarra, A., and D. Meloni, D.: Large atmospheric shortwave radiative forcing by
753   Mediterranean aerosol derived from simultaneous ground-based and spaceborne observations, and
754   dependence on the aerosol type and single scattering albedo, J. Geophys. Res., 115, D10209, doi:
755   10.1029/2009JD012697, 2010.

756 Di Biagio, C., Doppler, L., Gaimoz, C., Grand, N., Ancellet, G., Raut, J.-C., Beekmann, M.,
757   Borbon, A., Sartelet, K., Attié, J.-L., Ravetta, F., and Formenti, P.: Continental pollution in the
758   western Mediterranean basin: vertical profiles of aerosol and trace gases measured over the sea
759   during TRAQA 2012 and SAFMED 2013, Atmos. Chem. Phys., 15, 9611-9630, doi:10.5194/acp-
760   15-9611-2015, 2015.

761 Dubovik, O., Holben, B., Eck, T. F., Smirnov, A., Kaufman, Y. J., King, M. D., Tanré, D., and
762   Slutsker, I.: Variability of absorption and optical properties of key aerosol types observed in
763   worldwide locations, J. Atmos. Sci., 59, 590–608, 2002.

764 Dubuisson, P., Buriez, J. C. and Fouquart, Y.: High spectral resolution solar radiative transfer in
765   absorbing and scattering media: Application to the satellite simulation, J. Quant. Spectrosc. Radiat.
766   Transfer, 55, 103–126, 1996.

767 Dubuisson, P., Roger, J., Mallet, M., and Dubovik, O.: A Code to Compute the Direct Solar Radiative
768   Forcing: Application to An- thropogenic Aerosols during the Escompte Experiment, Proc. In-
769   ternational Radiation Symposium (IRS 2004) on Current Prob- lems in Atmospheric Radiation,
770   edited by: Fischer, H., Sohn, B.- J., and Deepak, A., Hampton, 127–130, 23–28 August 2004, Bu-
771   san, Korea, 2006.

772 Ebert, M., Weinbruch, S., Rausch, A., Gorzawski, G., Hoffmann, P., Wex, H., and Helas, G.: The
773   complex refractive index of aerosols during LACE 98 as derived from the analysis of individual
774   particles, J. Geophys. Res., 107, D21, 8121, doi:10.1029/2000JD000195, 2002.

775 Ebert, M., Weinbruch, S., Hoffmann, P., and Ortner, H. M.: The chemical composition and complex
776   refractive index of rural and urban influenced aerosols determined by individual particle analysis,
777   Atmos. Environ., 38, 6531–6545, 2004.

778 Estellés, V., Martínez-Lozano, J. A., Utrillas, M. P., and Campanelli, M.: Columnar aerosol properties
779   in Valencia (Spain) by ground-based Sun photometry, J. Geophys. Res., 112, D11201,
780   doi:10.1029/2006JD008167, 2007.

781 Esteve, A. R., Ogren, J. A., Sheridan, P. J., Andrews, E., Holben, B. N., and Utrillas, M. P.: Sources
782   of discrepancy between aerosol optical depth obtained from AERONET and in-situ aircraft
783   profiles, Atmos. Chem. Phys., 12, 2987-3003, doi:10.5194/acp-12-2987-2012, 2012.

784 Giorgi, F., and Lionello, P.: Climate change projections for the Mediterranean region. Global Planet
785   Change, 63, 90-104. doi:10.1016/j.gloplacha.2007.09.005, 2008.

786 Gkikas, A., Houssos, E. E., Hatzianastassiou, N., Papadimas C. D., and Bartzokas, A.: Synoptic
787   conditions favouring the occurrence of aerosol episodes over the broader Mediterranean basin Q. J.
788   R. Meteorol. Soc. 138: 932–949, 2012.

789 Hess, M., Koepke, P., and Schult, I.: Optical properties of aerosols and clouds: The software package
790   OPAC, Bull. Am. Meteorol. Soc, 79, 831–844, 1998.

791 Horvath, H., Alados Arboledas, L., Olmo, F. J., Jovanovic, O., Gangl, M., Sanchez, C., Sauerzopf, H.,
792   and Seidl, S.: Optical characteristics of the aerosol in Spain and Austria and its effect on radiative
793   forcing, J. Geophys. Res., 107, 4386, doi: 10.1029/2001JD001472, 2002.

794 IPCC, 2013: Climate Change 2013: The Physical Science Basis. Contribution of Working Group I to
795   the Fifth Assessment Report of the Intergovernmental Panel on Climate Change [Stocker, T.F., D.
796   Qin, G.-K. Plattner, M. Tignor, S.K. Allen, J. Boschung, A. Nauels, Y. Xia, V. Bex and P.M.
797   Midgley (eds.)]. Cambridge University Press, Cambridge, United Kingdom and New York, NY,
798   USA, 1535 pp, doi:10.1017/CBO9781107415324.

799   Jin, Z., Charlock, T. P., Smith Jr., W. L., and Rutledge, K.: A parametrization of ocean surface
800   albedo, Geophys. Res. Lett., 31, L22301, doi:10.1029/2004GL021180, 2004.

801   Lelieveld, J., Berresheim, H., Borrmann, S., et al.: Global air pollution crossroads over the
802   Mediterranean, Science, 298, 794–799, 2002.

803   Liu, Y. and Daum, P.: The effect of refractive index on size distributions and light scattering
804   coefficients derived from optical particle counters, J. Aerosol Sci., 31, 945–957, 2000.Loeb, N. G.,
805   and Su, W.: Direct Aerosol Radiative Forcing Uncertainty Based on a Radiative Perturbation
806   Analysis, J. Climate, 23, 5288–5293. doi: http://dx.doi.org/10.1175/2010JCLI3543.1, 2010.

807   Loeb, N. G., and Su, W. Y.: Direct aerosol radiative forcing uncertainty based on a radiative
808   perturbation analysis, J. Clim., 23, 5288–5293, 2010.

809   Lyamani, , H., Olmo, F. J., Alcántara, A., and Alados-Arboledas, L.: Atmospheric aerosols during the
810   2003 heat wave in southeastern Spain. I: Spectral optical depth, Atmos. Environ., *40*, 6453–6464,
811   2006.

812   Lyamani, H., Valenzuela, A., Perez-Ramirez, D., Toledano, C., Granados-Muñoz, M. J., Olmo, F. J.,
813   and Alados-Arboledas, L.: Aerosol properties over the western Mediterranean basin: temporal and
814   spatial variability, Atmos. Chem. Phys., 15, 2473-2486, doi:10.5194/acp-15-2473-2015, 2015

815   Mallet, M., Roger, J. C., Despiau, S., Dubovik, O., and Putaud, J. P.: Microphysical and optical
816   properties of aerosol particles in urban zone during ESCOMPTE, Atmos. Res., 69, 73–97, 15
817   2003.

818   Mallet, M., Van Dingenen, R., Roger, J. C., Despiau, S., and Cachier, H.: In situ airborne
819   measurements of aerosol optical properties during photochemical pollution events, J. Geophys.
820   Res., 110, D03205, doi:10.1029/2004JD005139, 2005.

821   Mallet, M., Gomes, L., Solmon, F., Sellegri, K., Pont, V., Roger, J. C., Missamou, T., and Piazzola, J.:
822   Calculation of key optical properties of the main anthropogenic aerosols over the Western French
823   coastal Mediterranean Sea, Atmos. Res., 101, 396–411, 2011.

824   Mallet, M., Dubovik, O., Nabat, P., Dulac, F., Kahn, R., Sciare, J., Paronis, D., and Léon, J. F.:
825   Absorption properties of Mediterranean aerosols obtained from multi-year ground-based remote
826   sensing observations, Atmos. Chem. Phys., 13, 9195-9210, doi:10.5194/acp-13-9195-2013, 2013.

827   McComiskey, A., Schwartz, S. E., Schmid, B., Guan, H., Lewis, E. R., Ricchiazzi, P., and Ogren, J.
828   A.: Direct aerosol forcing: Calculation from observables and sensitivities to inputs, J. Geophys.
829   Res., 113, D09202, doi:10.1029/2007JD009170, 2008.

830   Meloni, D., di Sarra, A., Pace, G., and Monteleone, F.: Aerosol optical properties at Lampedusa
831   (Central Mediterranean). 2. Determination of single scattering albedo at two wavelengths for
832   different aerosol types, Atmos. Chem. Phys., 6, 715-727, doi:10.5194/acp-6-715-2006, 2006.

833   Millán, M. M., Mantilla, E., Salvador, R., Carratala, A., Sanz, M. J., Alonso, L., Gangoiti, G., and
834   Navazo, M.: Ozone cycles in the western Mediterranean basin: interpretation of monitoring data in
835   complex terrain, J. Appl. Meteorol., 4, 487–507, 2000.

836   Müller, D., Ansmann, A., Wagner, F., Franke, K., and Althausen, D.: European pollution outbreaks
837   during ACE 2: Microphysical particle properties and single-scattering albedo inferred from
838   multiwavelength lidar observations, J. Geophys. Res., 107, D15, 4248, 10.1029/2001JD001110,
839   2002.

840   Nabat, P., Somot, S., Mallet, M., Sevault, F., Chiacchio, M. and Wild, M.: Direct and semi-direct
841   aerosol radiative effect on the Mediterranean climate variability using a coupled Regional Climate
842   System Model Clim. Dyn., 44, 1127-1155, doi:10.1007/s00382-014-2205-6, 2015.

843   Nedélec, P., Cammas, J.-P., Thouret, V., Athier, G., Cousin, J.-M., Legrand, C., Abonnel, C.,
844   Lecoeur, F., Cayez, G., and Marizy, C.: An improved infrared carbon monoxide analyser for
845   routine measurements aboard commercial Airbus aircraft: technical validation and first scientific

846   results of the MOZAIC III programme, Atmos. Chem. Phys., 3, 1551–1564, doi:10.5194/acp-3-
847   1551-2003, 2003.

848 Pace, G., di Sarra, A., Meloni, D., Piacentino, S., Chamard, P.: Aerosol optical properties at
849   Lampedusa (Central Mediterranean). 1. Influence of transport and identification of different
850   aerosol types, Atmos. Chem. Phys., 6, 697–713, 2006.

851 Pandolfi, M., Cusack, M., Alastuey, A., and Querol, X.: Variability of aerosol optical properties in the
852   Western Mediterranean Basin Atmos. Chem. Phys., 11, 8189–8203, 2011.

853 Pandolfi, M., et al.: Effects of sources and meteorology on particulate matter in the Western
854   Mediterranean Basin: An overview of the DAURE campaign, J. Geophys. Res. Atmos., 119,
855   4978–5010, doi:10.1002/2013JD021079, 2014.

856 Pérez, N., Pey, J., Castillo, S., Viana, M., Alastuey, A., and Querol, X.: Interpretation of the
857   variability of levels of regional background aerosols in the Western Mediterranean, Sci. Tot.
858   Environ., 407, 527–540, 2008.

859 Pey, J., Querol, X., and Alastuey, A.: Discriminating the regional and urban contributions in the
860   North-Western Mediterranean: PM levels and composition, Atmos Environ, 44, 1587–96, 2010.

861 Piazzola, J., Sellegri, K., Bourcier, L., Mallet, M., Tedeschi, G., and Missamou, T.: Physicochemical
862   characteristics of aerosols measured in the spring time in the Mediterranean coastal zone, Atmos.
863   Environ., 54, 545-556, 2012.

864 Ramana, M. V., and Ramanathan, V.: Abrupt transition from natural to anthropogenic aerosol
865   radiative forcing: Observation at the ABCMaldives Climate Observatory, J. Geophys. Res., 111,
866   D20207, doi:10.1029/2006JD007063, 2006.

867 Raut, J.-C., and Chazette, P.: Vertical profiles of urban aerosol complex refractive index in the frame
868   of ESQUIF airborne measurements, Atmos. Chem. Phys., 8, 901–919, 2008.Russell, P. B.,
869   Bergstrom, R. W., Shinozuka, Y., Clarke, A. D., DeCarlo, P. F., Jimenez, J. L., Livingston, J. M.,
870   Redemann, J., Dubovik, O., and Strawa, A.: Absorption Angstrom Exponent in AERONET and
871   related data as an indicator of aerosol composition, Atmos. Chem. Phys., 10, 1155–1169,
872   doi:10.5194/acp-10-1155-2010, 2010.

873

874 Russell, P. B., Bergstrom, R. W., Shinozuka, Y., Clarke, A. D., DeCarlo, P. F., Jimenez, J. L.,
875   Livingston, J. M., Redemann, J., Dubovik, O., and Strawa, A.: Absorption Angstrom Exponent in
876   AERONET and related data as an indicator of aerosol composition, Atmos. Chem. Phys., 10,
877   1155–1169, doi:10.5194/acp-10-1155-2010, 2010.

878 Saha, A., Mallet, M., Roger, J. C., Dubuisson, P., Piazzola, J., and Despiau, S.: One year
879   measurements of aerosol optical properties over an urban coastal site: Effect on local direct
880   radiative forcing, Atmos. Res., *90*, 195-202, 2008.
881 Stamnes K., Tsay, S. C., Wiscombe, W., and Jayaweera, K.: Numerically stable algorithm for
882   discrete-ordinate-method radiative transfer in multiple scattering and emitting layered media,
883   Appl. Opt., 27, 2502–2509, 1988.

884 Stier, P., Schutgens, N. A. J., Bellouin, N., Bian, H., Boucher, O., Chin, M., Ghan, S., Huneeus, N.,
885   Kinne, S., Lin, G., Ma, X., Myhre, G., Penner, J. E., Randles, C. A., Samset, B., Schulz, M.,
886   Takemura, T., Yu, F., Yu, H., and Zhou, C.: Host model uncertainties in aerosol radiative forcing
887   estimates: results from the AeroCom Prescribed intercomparison study, Atmos. Chem. Phys., 13,
888   3245-3270, doi:10.5194/acp-13-3245-2013, 2013.

889 Stohl, A., Hittenberger, M., and Wotawa, G.: Validation of the Lagrangian particle dispersion model
890   Flexpart against large-scale tracer experiment data, Atmos. Environ., 32, 4245–4264, 1998.

891

892 Toledano, C., Cachorro, V. E., Berjon, A., de Frutos, A. M., Sorribas, M., de la Morena, B. A., and
893   Goloub, P.: Aerosol optical depth and Ångstrom exponent climatology at El Arenosillo

AERONET site (Huelva, Spain), Q. J. Roy. Meteorol. Soc., 133, 795–807, doi:10.1002/qj.54, 2007.

Weingartner, E., Saathof, H., Schnaiter, M., Streit, N., Bitnar, B., and Baltensperger, U.: Absorption of light by soot particles: Determination of the absorption coefficient by means of Aethalometers, J. Aerosol Sci., 34, 1445–1463, 2003.

932 **Tables**

933

934 **Table 1.** Summary of information on the SLRs analysed in this study. The SLR location

935 (within the boundary layer or in the free troposphere) ~~has been~~was determined based on the

936 boundary layer top height estimated for the closest vertical sounding performed during each

937 flight (see Di Biagio et al., 2015). The ~~Sector~~ sector of origin for sampled air masses ~~has~~

938 ~~been~~was determined based on FLEXPART back-trajectories.

939

Flight number	SLR_ID	Date	Time start-stop	Altitude (m)	Location	Sector of origin
V19	V19_R1	26/06/2012	11:23-11:38	322	Within the boundary layer	Eastern
V19	V19_R2	26/06/2012	11:44-11:59	897	Within the boundary layer	Eastern
V21	V21_R1	27/06/2012	10:54-11:12	312	Within the boundary layer	Eastern
V21	V21_R2	27/06/2012	11:48-12:04	629	Within the boundary layer	Eastern
V21	V21_R3	27/06/2012	12:05-12:19	311	Within the boundary layer	Western
V22	V22_R1	29/06/2012	7:42-8:01	478	Within the boundary layer	Eastern
V23	V23_R2	29/06/2012	12:05-12:20	319	Within the boundary layer	Open sea
V25	V25_R1	04/07/2012	9:08-9:24	639	Within the boundary layer	Western
V25	V25_R2	04/07/2012	9:32-9:48	2015	Free troposphere	Western
V25	V25_R3	04/07/2012	9:50-10:08	2538	Free troposphere	Western
V26	V26_R2	04/07/2012	17:08-17:25	1877	Free troposphere	Western
V27	V27_R1	06/07/2012	9:28-9:47	164	Within the boundary layer	Open sea
V28	V28_R2	06/07/2012	15:58-16:13	927	Within the boundary layer	Open sea
V30	V30_R1	07/07/2012	14:09-14:28	3498	Free troposphere	Western
V30	V30_R2	07/07/2012	14:51-15:07	549	Within the boundary layer	Open sea
V31	V31_R1	10/07/2012	15:44-16:20	322	Within the boundary layer	Western
V31	V31_R2	10/07/2012	16:31-16:59	954	Within the boundary layer	Western
V32	V32_R1	11/07/2012	12:52-13:13	250	Within the boundary layer	Western
V32	V32_R2	11/07/2012	13:22-13:48	788	Within the boundary layer	Western
V32	V32_R3	11/07/2012	14:02-14:12	336	Within the boundary layer	Western
V32	V32_R4	11/07/2012	14:18-14:35	802	Within the boundary layer	Western

940

941

942 **Table 2.** Summary of the aerosol in situ measurements on the ATR-42 during the TRAQA

943 campaign. Details on the data treatment and uncertainty estimation for the different instruments are

944 provided in Sect. 2.

945

946

Property measured	Instrument	Location on aircraft	Flow rate (l min⁻¹)	Time resolution	Size range	Sensitivity or uncertainty	Comments
Aerosol number concentration	Condensation Particle Counter (CPC 3775)	in the cabin behind AVIRAD inlet	1.5	5 sec	0.004 – 3 µm	±10% (concentration)	
Aerosol size distribution	Passive cavity aerosol spectrometer probe (PCASP 100x)	aircraft fuselage, left side before the wing	0.06	1 sec	Nominally 0.1 – 3.0 µm Corrected for refractive index 0.10 – 4.47 µm	<±25% (diameter optical to geometric conversion) ±15% (concentration) (e.g., Highwood et al., 2012)	Aerosol concentration underestimated by 50% between 0.4 and 1.0 µm
	GRIMM 1.129	in the cabin behind AVIRAD inlet	1.3	6 sec	Nominally 0.3 – 32 µm Corrected for refractive index 0.28 – 65.80 µm (AVIRAD 50% cut-off efficiency at ~12 µm diameter)	<±25% (diameter optical to geometric conversion) ±10% (concentration)	Data not available >350 m
Dry aerosol scattering coefficient σ_s (450, 550, 700 nm)	TSI 3563 integrating nephelometer	in the cabin behind AVIRAD inlet	30	6 sec	50% cut-off efficiency at ~12 µm diameter	<±10% for σ_s at 450, 550, and 700 nm	
Aerosol absorption coefficient (σ_a) (370, 470, 520, 590, 660, 880, 950 nm)	Magee AE31 aethalometer	in the cabin behind AVIRAD inlet	13	2 min	50% cut-off efficiency at ~12 µm diameter	11-70% variable at the different wavelengths	Data available only for 60% of SLRs

947

948

949

950

951 **Table 3.** Lognormal mode parameters of the measured aerosol size distribution (total aerosol
952 number concentration, N_{tot}, median diameter, D_g, and geometric standard deviation, σ_g). Data
953 corresponds to SLRs below ~350 m altitude. Diameters are given in microns and number
954 concentrations refer to ambient conditions.

955

		Mode 1	Mode 2	Mode 3	Mode 4	Mode 5	Mode 6	Mode 7
V19_R1	N_{tot}	498~~.00~~	160~~.00~~	~~20~~12.00	4.~~0.5~~0	1.~~9~~56	0.~~1~~04	
	D_g	0.13	0.24	0.38	0.6~~6~~1	1.55	4.85	
	σ_g	1.19	1.16	1.17	1.29	1.60	1.4~~53~~8	
V21_R1	N_{tot}	600~~.00~~	210~~.00~~	2~~.~~09.00	5.5~~0~~	0.5~~6~~5		
	D_g	0.13	0.24	0.37	0.5~~2~~48	1.3~~5~~56		
	σ_g	1.20	1.17	1.15	1.40	1.62		
V21_R3	N_{tot}	600~~.00~~	195~~.00~~	230.0~~7~~0	23.8~~00~~	0.48~~5~~0	0.0~~2~~01	
	D_g	0.13	0.23	0.3~~5~~7	0.5~~7~~1	1.4~~5~~5	4.5~~9~~50	
	σ_g	1.19	1.1~~6~~21	1.18	1.3~~8~~33	1.66	1.41	
V23_R2	N_{tot}	660~~.00~~	195~~.00~~	25~~.~~00	3.2~~0~~	0.75~~8~~0	0.0~~3~~2	
	D_g	0.13	0.23	0.37	0.5~~7~~3	1.4~~5~~59	5.69	
	σ_g	1.19	1.16	1.16	1.37	1.6~~5~~9	1.2~~5~~33	
V27_R1	N_{tot}	930~~.00~~	264~~.00~~	40.00~~2.5~~	45.6~~2~~0	0.5~~2~~70	0.04	0.004
	D_g	0.13	0.23	0.37	0.4~~8~~55	1.3~~0~~57	3.~~.8~~50	8.20
	σ_g	1.19	1.1~~7~~20	1.18	1.4~~0~~38	1.68	1.12	1.26
V31_R1	N_{tot}	482~~.00~~	278~~.00~~	48~~.00~~	2.7~~0~~	0.55	0.01	
	D_g	0.14	0.24	0.35	0.54	1.82	7.14	
	σ_g	1.20	1.16	1.17	1.39	1.65	1.17	
V32_R1	N_{tot}	1135~~.00~~	413~~.00~~	55~~.00~~	5.0~~0~~	0.65	0.01	
	D_g	0.13	0.23	0.37	0.50	1.65	7.30	
	σ_g	1.19	1.18	1.16	1.37	1.66	1.11	
V32_R3	N_{tot}	235~~.00~~	84~~.00~~	128~~.00~~	1.80~~3.2~~	0.1~~2~~15	0.02	0.~~004~~002
	D_g	0.14	0.2~~3~~8	0.3~~2~~8	0.4~~5~~0	1.4~~2~~57	3.7~~5~~29	7.9~~9~~21
	σ_g	1.19	1.16	1.16	1.3~~2~~32	1.68	1.12	1.31

956

957

958

959 **Table 4.** Maximum, mean, and minimum of the single scattering albedo considered for radiative
960 transfer calculations. Values are reported at the 7 wavelengths used as inputs in the GAME model.

	330 nm	400 nm	550 nm	670 nm	870 nm	1020 nm	1500 nm
SSA max	0.98	0.98	0.99	0.99	1.00	0.99	0.99
SSA mean	0.93	0.93	0.92	0.91	0.90	0.90	0.89
SSA min	0.88	0.87	0.85	0.85	0.83	0.82	0.80

961

962

963

964

Figures

Figure 1. Upper panel: geographical position of the different straight levelled runs (SLRs) performed during the TRAQA campaign and analysed in this paper. The label for each point in the figure identifies the flight number and the corresponding SLR: for example V22_R1 indicates the coordinates of the first SLR of flight V22. Lower panel: definition of three different source areas for the various SLRs (see Sect. 3.~~1~~ 4 for more details). The Western sector includes trajectories coming from the Atlantic Ocean and travelling over France or northern Spain before reaching the Western basin; the Eastern sector includes air mass trajectories from continental Europe that have travelled over northern Italy-Po Valley before entering the basin; and the Open sea sector consists of trajectories which have experienced at least 2 days of subsidence over the sea in the Western basin.
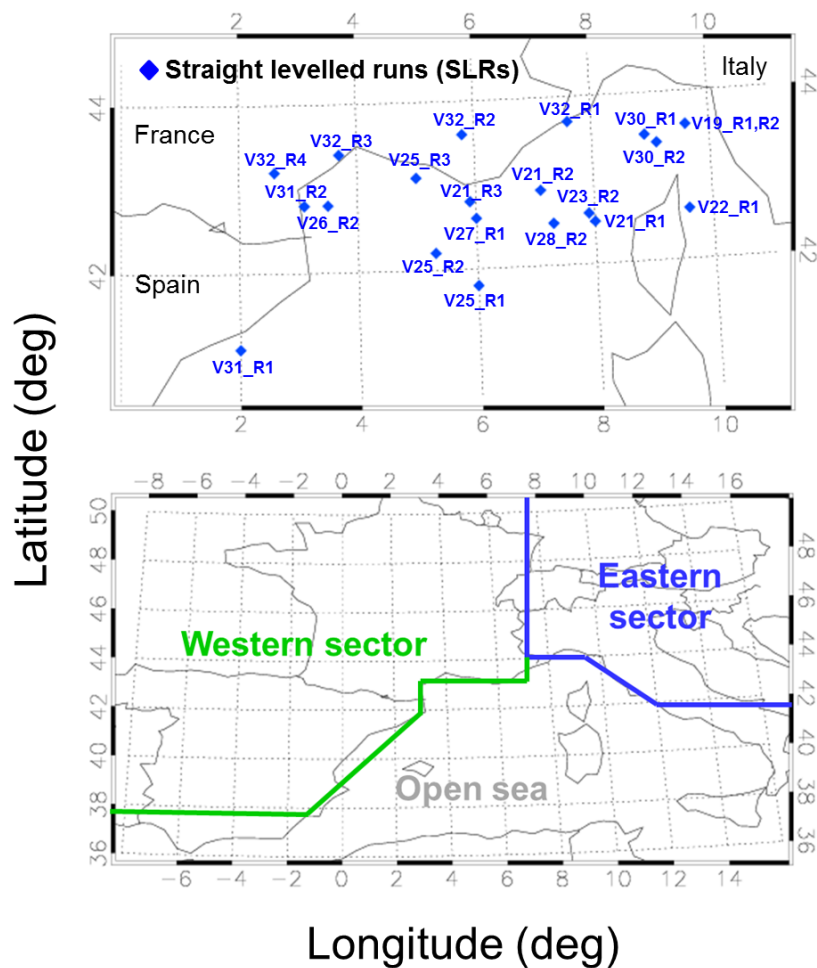
981   **Figure 2.** Flowchart of the size distribution and refractive index retrieval procedure. Further details

982   are provided in Sect. 3.2.

983
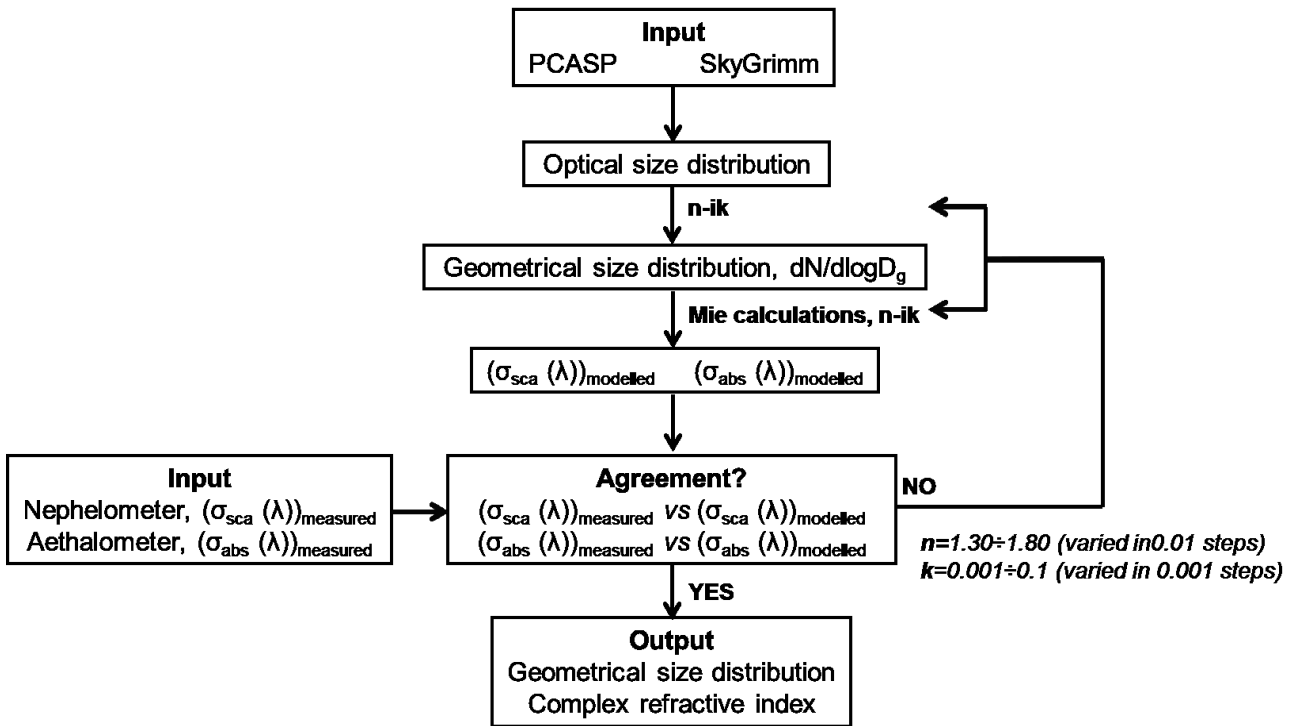
984

985

986

987

988

989

990

991

992

993

994

995

996

997

998

999

1000

Figure ~~2~~3. Averages over the different TRAQA straight levelled runs (SLRs) of the measured: altitude, spectral scattering coefficient (σ_s; 450, 550, and 700 nm), scattering Ångström exponent (SAE), spectral absorption coefficient (σ_{abs}; 370, 470, 520, 590, 660, 880, and 950 nm), absorption Ångström exponent (AAE), ozone enhancement factor ($\Delta O_3/\Delta CO$) and ~~Aitken~~ultrafine-to-accumulation ratio ($dN_{\text{\sout{Aitken}UFP}}/dN_{Acc}$). Uncertainties indicate the 1-σ standard deviation. The x-axis indicates the flight number (19 to 32 for flights V019 to V032); each point for the same flight number represents a different SLR.
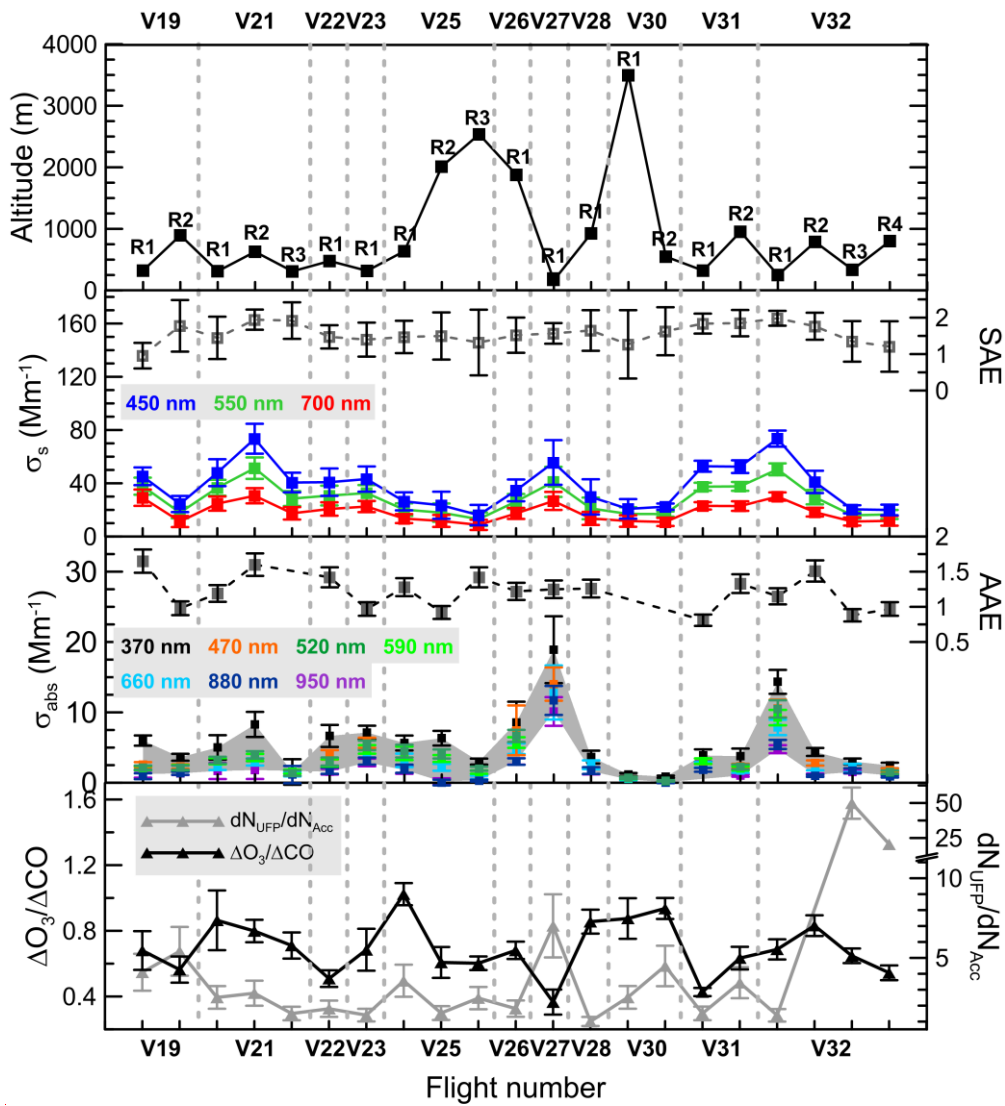
Figure ~~3~~4. Number size distributions (left panel) and volume size distributions (right panel) measured over the different SLRs for the TRAQA flights. Data corresponds to measurements performed within the boundary layer at altitudes <350 m (V19_R1, V21_R1, V21_R3, V23_R2, V27_R1, V31_R1, V32_R1, V32_R3). Data are separated based on the different air mass origin (Western sector, Eastern sector, and Open sea). Concentrations are given at ambient conditions. Grey shading represents minimum and maximum measured values, while the black curve is the average size. Measurement uncertainties are also reported for the average curve.
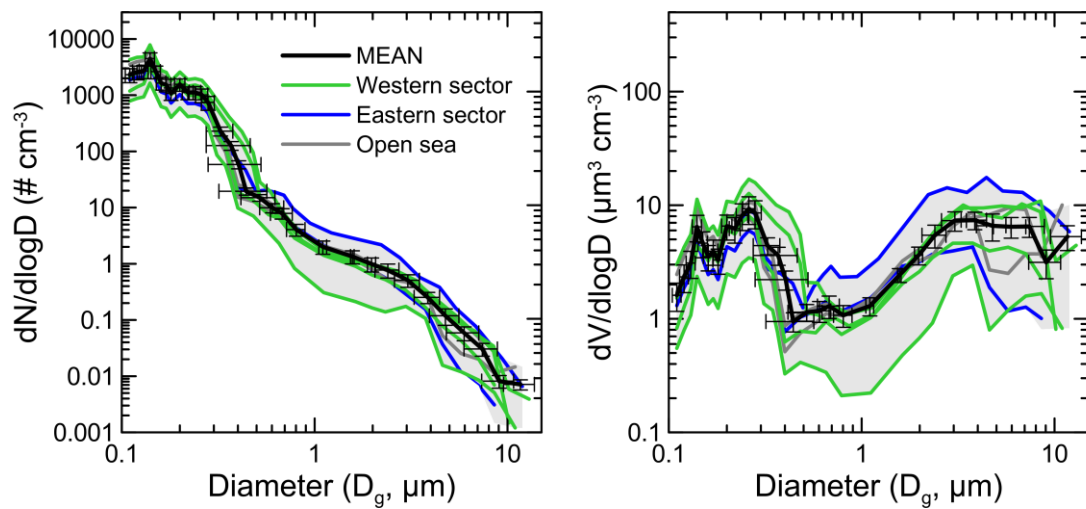
Figure 45. Spectral single scattering albedo at seven wavelengths between 370 and 950 nm calculated from nephelometer and aethalometer measurements for the different SLRs within pollution layers. Data are separated based on the different air mass origin (Western sector, Eastern sector, and Open sea).
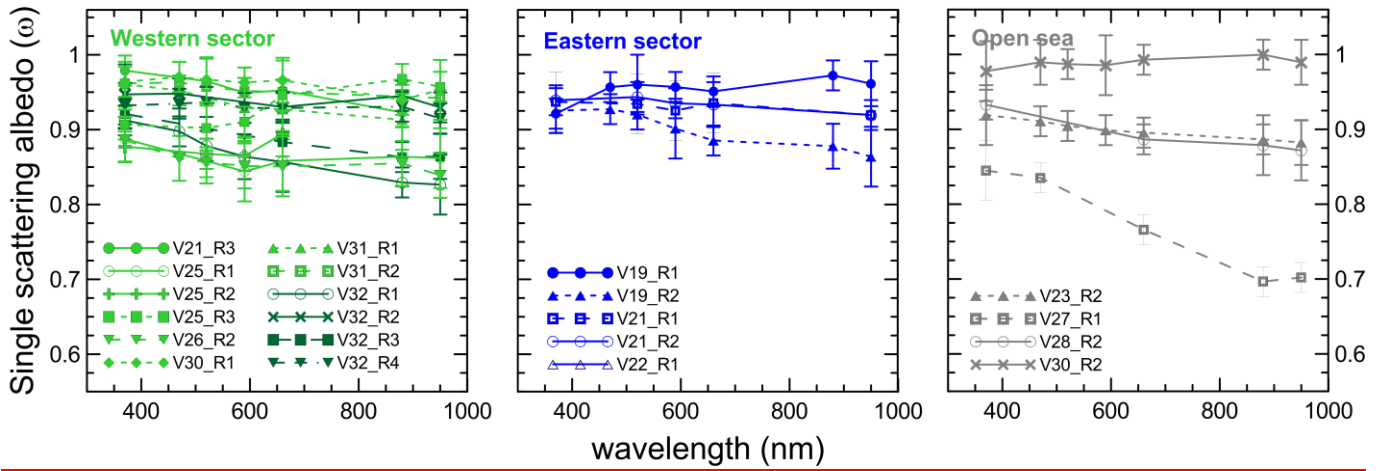
Figure ~~5~~6. Single scattering albedo (370, 660, and 950 nm), ozone enhancement factor ($\Delta O_3/\Delta CO$), ~~Aitken~~ultrafine-to-accumulation ratio ($dN_{\text{Aitken}UFP}/dN_{Acc}$), and scattering (SAE) and absorption Ångström exponent (AAE) versus height for all analysed SLRs cases. Uncertainties on measured and retrieved quantities (horizontal bars) are also shown in the plots.
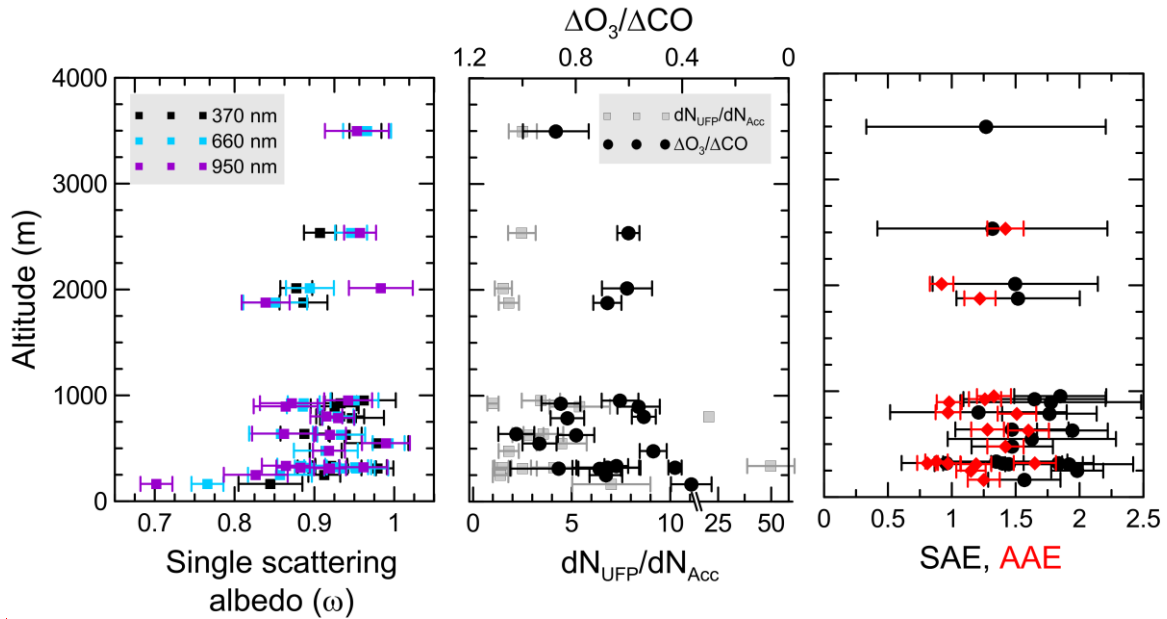
1087 **Figure 6~~7~~.** Comparison of the aerosol scattering (σ_s, left panel) and absorption (σ_{abs}, right panel)

1088 coefficients measured by the nephelometer and the aethalometer and calculated from measured size

1089 distribution data with Mie theory. Data are given at ambient conditions. Uncertainties on the

1090 measured (horizontal bars) scattering and absorption coefficients are also shown in the plots.

1091

1092
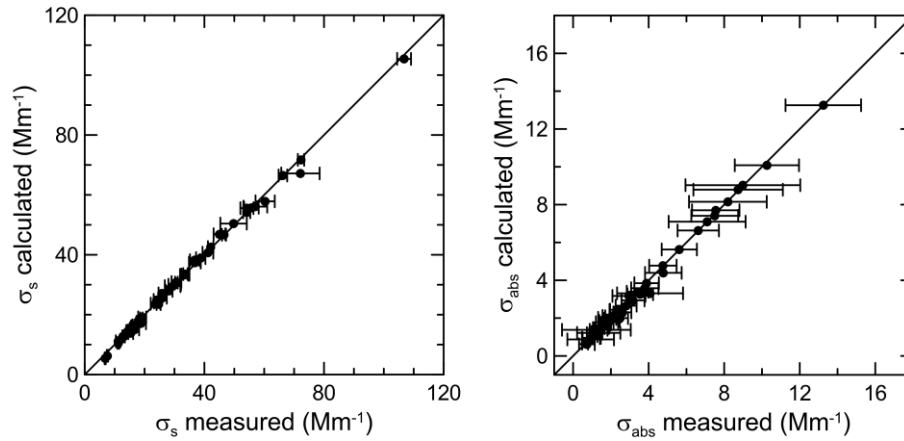
1093

1094

1095
1096

1097

1098

1099

1100

1101

1102

1103

1104

1105

1106

1107

1108

1109

1110

1111

1112

1113   **Figure 78.** Spectral real (n, left panel) and imaginary (k, right panel) parts of the complex refractive

1114   index obtained by optical closure for the 8 selected case studies. For sake of clarity, uncertainties on

1115   n and k are not reported in the plot. The values of the single scattering albedo measured at 370 and

1116   950 nm for the different cases are reported in the legend. The spectral real and imaginary parts of

1117   the complex refractive index as obtained from the Optical Properties of Aerosols and Clouds

1118   (OPAC, Hess et al., 1998) database for insoluble, water soluble, soot and sea salt components are

1119   also reported in the plot. These components are used in OPAC to model continental polluted,

1120   continental rural, urban, and maritime polluted aerosols.

1121
1122

1123
1124
1125
1126
1127
1128
1129
1130
1131
1132
1133
1134
1135
1136
1137
1138
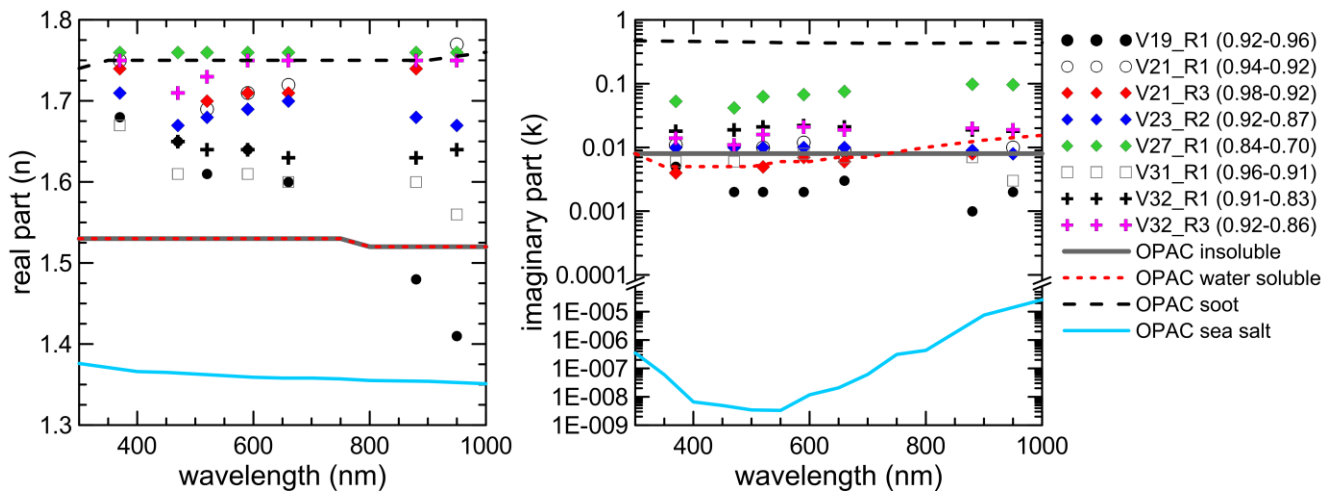
1139 **Figure 8_9_.** Spectral single scattering albedo plotted against the real (left panel) and the imaginary
1140 (right panel) parts of the complex refractive index. The results of the linear fit between ω and k are
1141 reported in the legend. The fits are performed for the whole ω-k dataset, and also eliminating the
1142 data in correspondence of V27_R1, for which the largest values of k were observed.
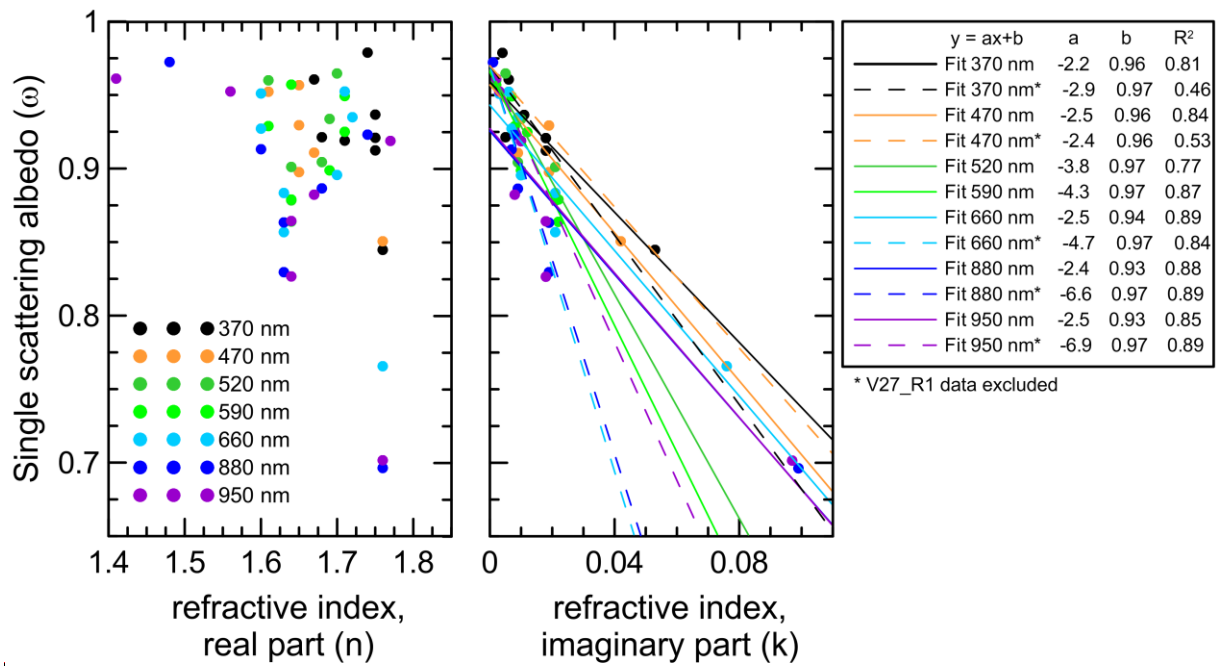
1161 **Figure 910.** Aerosol shortwave forcing efficiency at 60° solar zenith angle calculated at the surface,

1162 TOA, and within the atmosphere for the maximum, mean, and minimum of the single scattering

1163 albedo (ω) observed in this study (Table 4).

1164

1165